TECHNICAL UNIVERSITY OF LIBEREC

Faculty of Mechatronics and Interdisciplinary
Engineering Studies

DIPLOMA THESIS

Optical concentrators for Čerenkov light detector

**Systém pro soustředění světla v detektoru
Čerenkovova záření**

Supervisor: Doc. RNDr. Miroslav Šulc Ph.D (TUL)

Consultant: Dr. Silvia Dalla Torre (INFN Trieste)

Liberec 2005   Daniel Kramer

Abstrakt

Detektor RICH1 (Ring Imaging Čerenkov) je důležitou součástí experimentu čističové fyziky v CERN. Centrální část detektoru fotonů, původně plynového typu s fotokatodou z CsI, bude vyměněna za pole velmi rychlých vícekanálových fotonásobičů firmy Hamamatsu s rozšířenou citlivostí v UV oblasti.

Fotonásobiče mají cca. 3krát menší aktivní plochu než je nutné pokrýt, proto jsou vyžadovány optické koncentrátory transformující obraz z fokální roviny původního systému na novou fotokatodu. Soustava musí mít dostatečnou účinnost v rozmezí 200 až 600nm a úhlovou akceptantci pro paprsky vytvořené většinou zajímavých fyzikálních událostí systému. Bylo navrženo několik typů designu (např. dutý vlnovod) a zvolen „teleskopický" asférický koncept se dvěma čočkami pro svou prokázanou funkčnost v experimentu HERA-B. Jako materiál byl zvolen tavený křemen v UV kvalitě. Soustava je složena z plankonvexní polní čočky ve fokální rovině zrcadel detektoru a bikonvexní čočky kondenzoru.

Nejprve byl navržen plně asférický systém s nejlepší kvalitou zobrazení a poté snižována zobrazovací kvalita i výrobní cena při zachování požadavků experimentu. Fyzikální model prokázal nutnost vertikálního náklonu systému, technicky možného jen částečně, proto je polní čočka navržena prizmatická a kondenzorová čočka je nakloněná a decentrovaná.

Výkonnost systému byla testována metodou Monte-Carlo, což umožnilo vhodnější optimalizaci. Testování pomocí paprsků z komplexní simulace detektoru ukázalo na nutnost náklonu také v horizontální rovině.

Hotový design je připraven pro výrobu a splňuje všechny optické, rozměrové, mechanické a rozpočtové požadavky.

Abstract

RICH1 (Ring Imaging Cherenkov) detector is an important part of COMPASS particle physics experiment in CERN. Its central area photon detection part is being upgraded from wire chambers with CsI layers to very fast UV extended Hamamatsu MAPMTs (Multi Anode Photo Multiplier Tubes) array. MAPMTs have approx. 3 times smaller active area than the covered region, thus optical concentrators transforming image from old system focal plane to the new photocathode were needed. System was expected to be efficient

from 200 to 600nm with best performance at 300nm and with angular acceptance including all interesting physics processes. Several design types (including i.e. a hollow waveguide) were investigated and the "telescopic" two lens aspherical design concept was selected for its proven functionality in HERA-B experiment. Chosen material was UV grade fused silica. System consists of a field lens placed in the focal plane of the RICH mirrors and a condenser lens downstream. Designing procedure started with a high optical quality fully aspherical system and continued by a gradual decrease in imaging performance to match the budget but still satisfy the physics requirements. Particle simulations showed a necessity of the system tilt but mounting constraints didn't fully allow it, so the field lens was made prismatic with one flat side and the condenser lens off centered and tilted. Performance of the designs was tested by Monte Carlo method allowing a better optimization. Testing by rays from complex detector simulation implied a necessity of tilt in another plane. Design ready for production satisfies all performance, dimensional, mounting and cost expectations.

Contents

1 Introduction

COMPASS (COmmon Muon Proton Apparatus for Symmetry and Spin) setup is the largest fixed target particle physics experiment in CERN (European Organization for Nuclear Research). During the year 2005, several of its subsystems undergo major upgrades targeted mainly to the response increase.

RICH1 (Ring Imaging Čerenkov Detector) is used for particle identification by measuring the velocity by means of emitted Čerenkov light transformed into circles, composed of just few photons each. Wire-chambers with CsI layers used in the past as photon detectors are going to be replaced by an array of much faster MAPMTs (Multi-Anode Photomultiplier Tubes).

As the active area of the MAPMTs is smaller than the one to be covered, one needs a concentrator optical system to minimize the dead areas. The Čerenkov photon production is rapidly increasing with light frequency, so the concentrators should have the best performance in the near UV region and agree with the quantum efficiency of the MAPMTs. The system should have a maximized acceptance of the incoming "interesting" photons with respect to their angular distributions (including an average tilt in the vertical plane). It is very important to respect the limited available space for the optics imposed by the electronics and mechanics of other parts of the detector.

1.1   Objectives

Target of this work is to design and optimize the concentrator optics according to the given targets and specifications, test its performance by means of the Monte Carlo tools and choose safe production tolerances. The design should be made in close cooperation with other detector groups and industry.

1.2   COMPASS experiment at CERN

The COMPASS apparatus is a large particle physics experiment in CERN using a high intensity SPS (Super Proton Synchrotron) beam of polarized muons (or hadrons) interacting with two fixed targets composed of Li_6D. The nucleons inside the target material are polarized to a certain level and the target is kept at cryogenic temperatures (5mK) inside a solenoid or dipole magnet.

The system uses two spectrometer magnets to deviate charged particles and several types of particle detection systems to enable high precision particle tracking in space and time, electromagnetic and hadronic calorimetry and muon detection, thus forming a very complex state-of-the-art setup. The RICH1 is the essential detector for the complex particle identification.

One of the main purposes of COMPASS muon beam program is the determination of the nucleon spin structure.
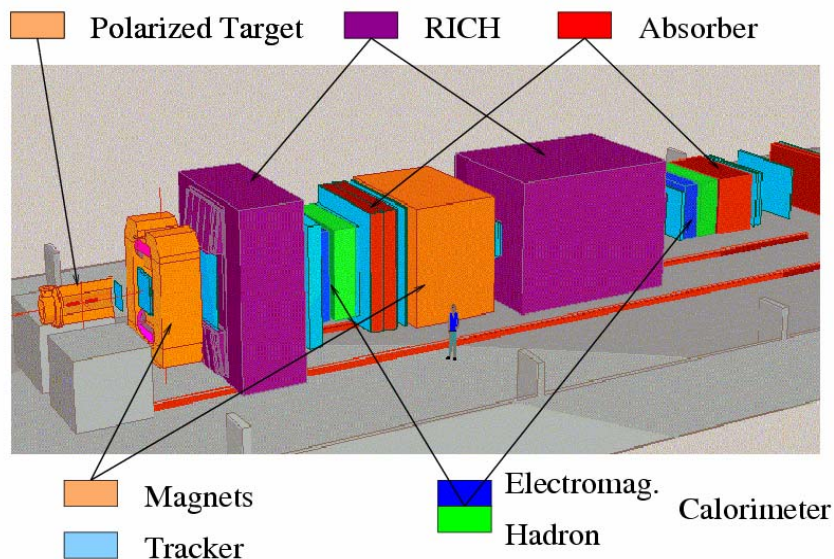
Figure 1.1: *Artistic drawing of the COMPASS setup including future RICH2 (larger purple box). From [2].*

2 Čerenkov radiation detection

2.1 Properties of the Čerenkov light

In 1934, it was discovered by P. A. Čerenkov that particles moving through the dielectric media faster than the local phase velocity of light emit a faint electromagnetic radiation at an angle related to the index of refraction of the media. The related theory was then formulated by I. M. Frank and I. J. Tamm in 1936 by means of classical electrodynamics.

If the charged particle moves at the conditions stated above, it can emit Čerenkov radiation with the constant conical wavefront with angle θ_c depending only upon its velocity and the index of refraction of the medium:

$$\cos\theta_C = \frac{1}{n(\lambda)\beta} + \left(\frac{\hbar}{\lambda p}\frac{n^2-1}{2n^2}\right) \quad (2.1)$$

where $\beta=\dfrac{c}{v}$ with c as light velocity in vacuum; the term in braces is a quantum mechanics correction but "completely negligible for any practical application" [1].

Because $\left|\cos\theta_C\right| \leq 1$, the phenomenon occurs only above a certain velocity and thus an energy threshold:

$$\gamma_t = \left(1-\frac{1}{n^2}\right)^{-\frac{1}{2}} \quad (2.2)$$

where $\gamma_t = \dfrac{E}{mc^2}$ with m as rest frame mass and E the particle's energy.
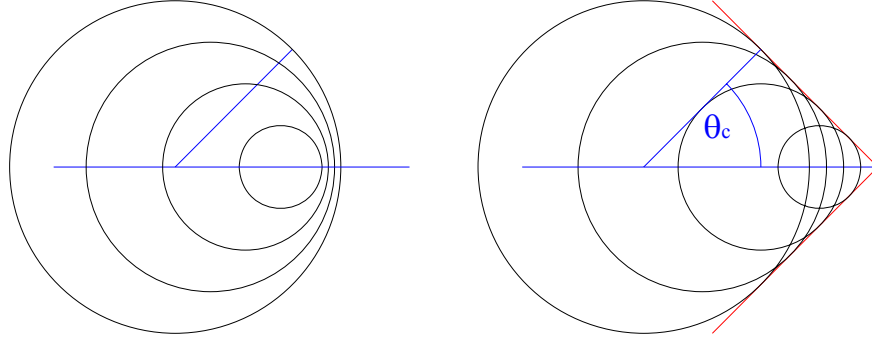
Figure 2.1: *Wavefronts determined by Huygens principle for $\gamma<\gamma_t$ (on the left) and $\gamma>\gamma_t$ building up the coherent wavefront cone (red).*

Assuming the limit velocity $\beta \to 1$, one gets the maximum possible Čerenkov angle:

$$\theta_{C\,max} = \arccos\frac{1}{n} \qquad (2.3)$$

The described properties are crucial for practical particle identification. Upon detection of a Čerenkov photon, one knows it comes from a charged particle above the threshold energy and its emission angle is defined by the velocity.

The spectral dependence of Čerenkov radiation energy integrated over the radiating path L can be described by:

$$\frac{dW}{d\omega} = \frac{LZ^2e^2\omega}{c^2}\left(1 - \frac{1}{\beta^2 n^2(\omega)}\right) \qquad (2.4)$$

with W as the radiated energy, ω the light frequency and Z the particle charge.

Assuming the photon energy $\hbar\omega$ one can get the number of emitted photons:

$$N = 2\pi LZ^2\alpha \int\limits_{\beta n>1}\left[1 - \left(\frac{\beta_t(\lambda)}{\beta}\right)^2\right]\frac{d\lambda}{\lambda^2} \qquad (2.5)$$

with α as fine structure constant and λ the photon wavelength. From this equation one could determine (thanks to $d\lambda/\lambda^2$), that the photons will be emitted mostly in the UV range.

After a small transformation of (2.5) and assuming $\beta \to 1$, the average number of photons per 10cm and 1eV frequency band gives:

$$N = 370Z^2\left(1 - \frac{1}{n^2}\right) \qquad (2.6)$$

One can see, that N is independent of the particle mass and as the Čerenkov effect is a statistical process, N is the "mean of the Poisson distribution in the number of photons" [1].

Čerenkov light has a full linear polarization in the plane defined by the particle track and the photon position.

2.2 RICH detector principle

The Ring Imaging CHerenkov detectors are the key instruments in particle identification for many recent particle physics experiments. They are used for the relatively high angular acceptance of the Čerenkov light and for the ability to allow simultaneous detection of photons from multiple events.

RICH detector is in principle an optical instrument with a radiator medium and focusing optics (spherical or parabolic mirrors). Proximity focusing RICH uses only a thin layer of high refraction material and in principle doesn't need any focusing mirrors, but this system will not be considered in this work.

RICH devices of COMPASS type are using large vessels filled with a radiator gas and a structure of mirrors transforming the Čerenkov light cones into the spherical wavefronts focalized onto the system of photon detectors in the mirrors focal plane.

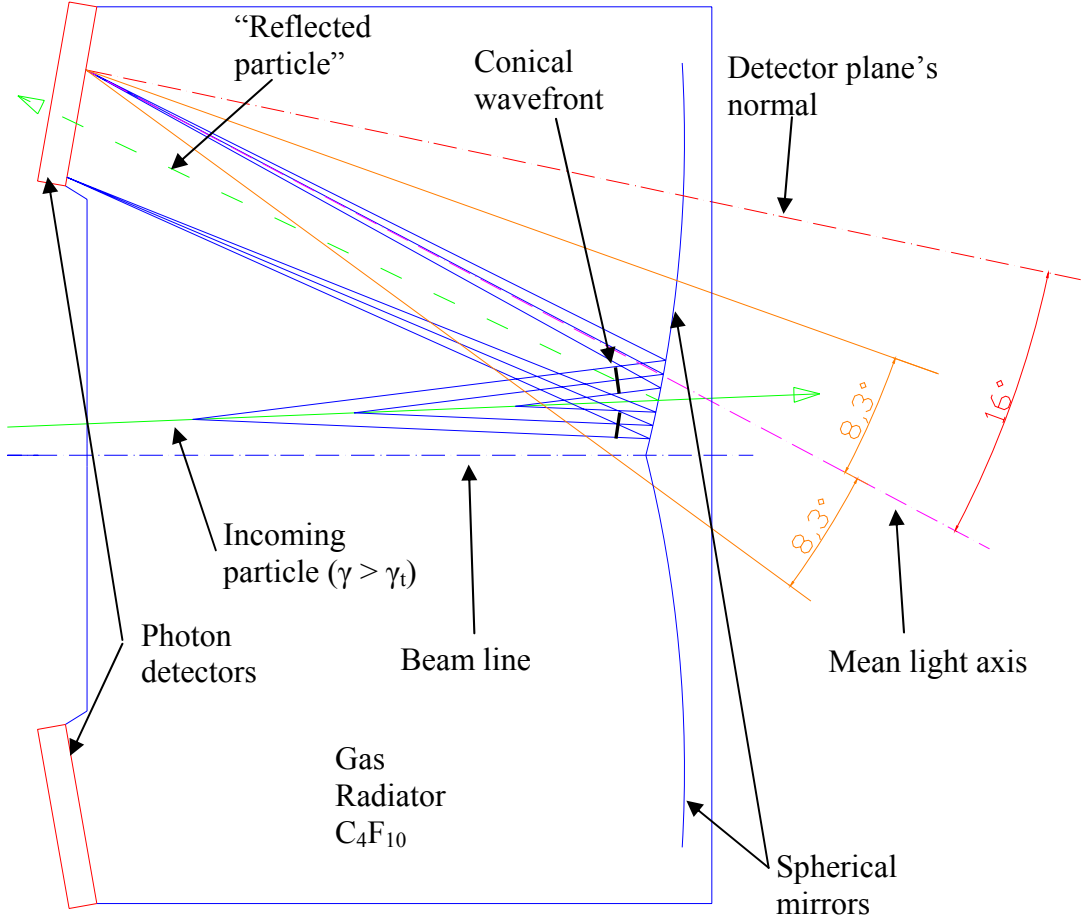The resulting ring radius r can be expressed as:

$$r = f \cdot \tan \theta_C \qquad (2.7)$$

with f the mirrors focal length [3].

Knowing the particle momentum, one can then compute the corresponding mass:

$$m = p\sqrt{n^2 \cos^2 \theta_C - 1} \qquad (2.8)$$

Attachment to the Diploma Thesis: Correction of the Figure 2.2

Figure 2.2: *Schematic cross section of COMPASS RICH1 detector with Čerenkov light cone (blue) transformed into a ring on the photo-detector plane, which is centered around the virtually reflected particle. The angular acceptance of the final is in orange.*

The particle mass is generally measured with the precision:

$$\left(\frac{dm}{m}\right)^2 = \left(\gamma^2 \frac{d\beta}{\beta}\right)^2 + \left(\frac{dp}{p}\right)^2 \qquad (2.9)$$

"If the momentum p is relatively well measured, then the resolution of particles with masses m_1 and m_2 requires a velocity resolution, $\Delta\beta$, given by" [1]:

$$\frac{\Delta\beta}{\beta} \cong \frac{m_1^2 - m_2^2}{2p^2} \qquad (2.10)$$

3 Design concept

3.1 RICH1 detector upgrade

The detector designed in mid 90s is used for hadron identification up to ~60GeV/c. Its angular particle acceptance is ±250 mrad in the horizontal and ±180 mrad in the vertical plane. The photon detection part is equipped with 8 Multi Wire Proportional Chambers (**MWPC**) [4] with large size CsI photocathodes allowing the single photon detection. The sensitive area covers 5.3 m^2 in total.

The photocathode material (array of 78x78 pads segmented to 8x8 mm^2) is very sensitive to contamination, so it must be operated in a methane atmosphere, separated from the radiator gas by a VUV transparent fused silica window. According to the CsI quantum efficiency, the system operates in the wavelength range 165 – 200 nm.

The future increase of the SPS beam luminosity and the need to suppress the background noise created by the beam halo will require much higher repetition rate of the photon detection. The present setup has a combined (electronics & detector) memory of cca 3μs, so the photon detector and the readout electronics upgrade is needed.
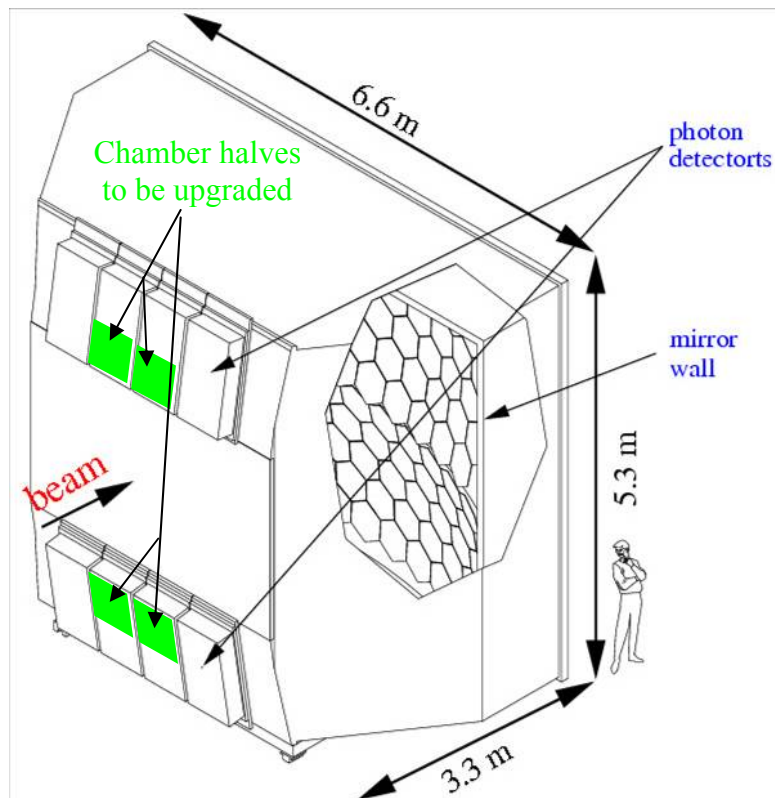
Figure 3.1: *Artistic view of RICH1 detector with 4 halves of MWPC chambers, which will be replaced by MAPMT arrays. From [10].*

It was decided to use the multianode photomultipliers recently developed by Hamamatsu. First tests showed a memory effect of cca 5ns [7]. Only the central part of the sensitive area having the highest occupancies because of the beam proximity will be replaced. The remaining halves of the chambers will be unchanged including the installed electronics, which can not be moved.

The R7600-03-M16 type has an 18x18 mm^2 bialkali photocathode segmented to 16 pads and a special borosilicate window with the UV transparency extended down to 200 nm. The area covered by one photomultiplier will be 48x48 mm^2 and 12x12 MAPMTs will be placed in each of four specially designed frames. It is planned to produce cca 600 systems to have some spare elements.
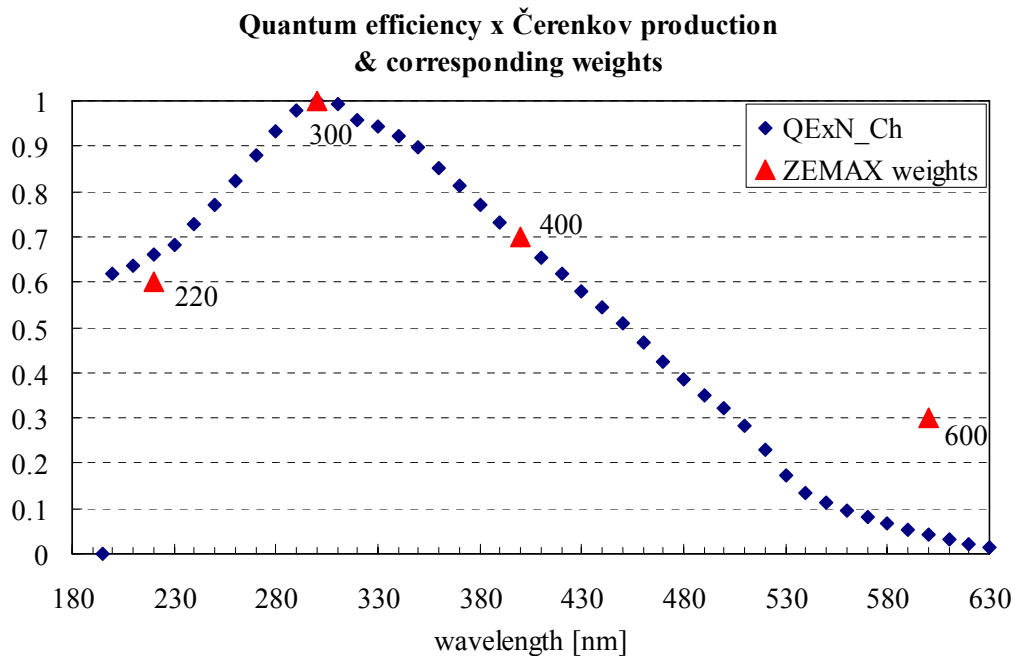
Figure 3.2: *Normalized plot of the MAPMT photoelectron conversion quantum efficiency multiplied by the number of Čerenkov photons (from Eq.2.6) produced by one particle (in blue) and corresponding weights used in the Zemax code (in red).*

The weights shown on the Fig. 3.2 were later used in all design optimizations and simulations. The last red point doesn't agree with the calculated data because of the need to increase the optimization stability. No point was used at 200 nm, because the dispersion formula for the fused silica material was not defined in the computer code.

3.2 Design targets and specifications

The RICH1 concentrators will be used together with the low resolution MAPMT, thus very high precision optics is not required. Nevertheless its wide UV range, large angular acceptance and the mechanical constraints make the design rather challenging.

Basic specifications are summarized in the following table:

Wavelength range	200..600nm
Best performance at	300nm
Mean angle of rays to the detector plane normal	16°
Mechanically allowed tilt	11°
Incident light angular distribution standard deviation σ_H	3.3°
System length	minimized
Dead areas	minimized
Entrance window*	48x48mm^2
MAPMT active area	18x18mm^2
Angular acceptance	$> 2\ \sigma_H$
Image magnification (absolute value)	0.375
Focalization precision	$> 90\%$
Budget (600 systems)	120 k€
Final design deadline	March 2005

Table 3.1: *Basic RICH1 concentrators design requirements and specifications. The focalization precision will be defined in chapter 5. The entrance window is not necessarily square for the tilted design.*

It is important to underline, that one has to build cca 600 systems in 4 separated arrays, which will be surrounded by the old MWPCs in the transverse direction and by the electronics and the preceding detectors in the longitudinal. The design must be imperatively discussed with the producers of the mechanical housing and electronics and of course also with the potential producers of the lenses.

The system magnification is defined simply by dividing the entrance window's size by the photomultiplier's active area (18/48 = 0.375). If the design doesn't allow the square window size, the magnification would be matched to the longer side (48mm).
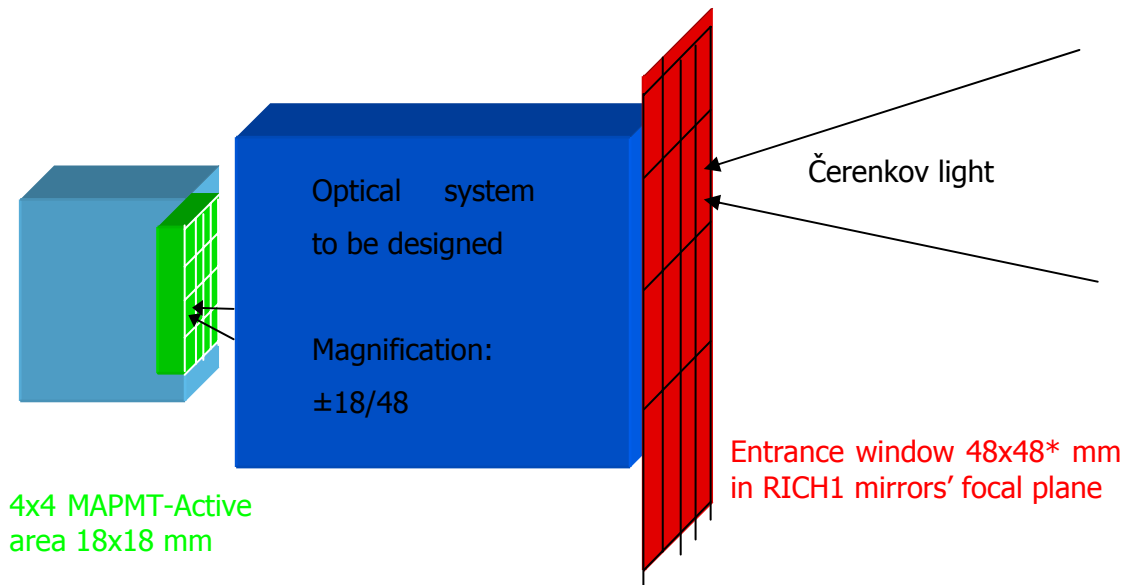
Figure 3.3: *Scheme showing the principle of concentrator optics for the case with negative magnification. Čerenkov rings are formed on the red plane.*

Schematic *Figure 3.3* shows only the straight type design, which would have to be tilted in the vertical plane by cca 16° to have its axis collinear with the mean axis of the incident Čerenkov light. For a centered system, such approach is not mechanically possible.
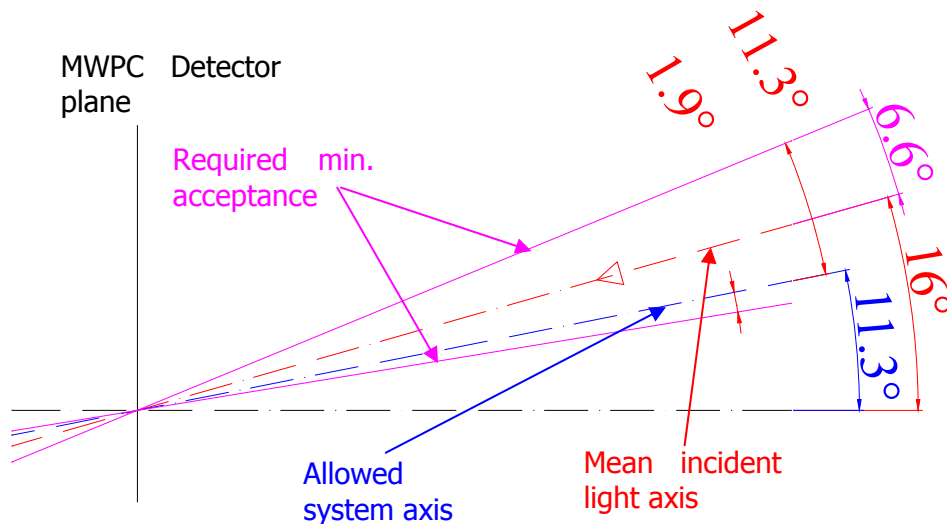
Figure 3.4: *Vertical projection showing the angular requirements of a straight system tilted to the blue axis. Resulting system acceptance would have to be +11.3° / -1.9°.*

The angular acceptance from the *Table 3.1* was used only as a first approximation and applies also to the *Figure 3.4*. Nevertheless, the complex COMPASS Monte Carlo simulations later showed a necessity to have the angular acceptance of at least 2.5σ in the horizontal plane.

3.3 Proposed solutions

Four different design conceptions were proposed and a short feasibility study was performed for each of them.

3.3.1 "Mushroom" type lens

The thick lenses solution with a cylindrical extension was already tested by the Trieste RICH group [7]. Lenses were produced by the Sol-Gel Novara [5] technology from a silica (SiO_2) substrate.

A grid of thick lenses was successfully tested also for the LHCb RICH detector [12].

The main inconvenience of the lenses for our case is the dead area they form in the corners of the square entrance window. As one needs cca 2.7times image demagnification, the resulting radius of curvature is so small, that the lens can't fill the whole aperture. Moreover, at the edges of the lens, the incident angle was close to 90° due to the high surface curvature, so the reflectivity was approaching 100% (*see Fig. 3.1*). The resulting losses due only to the limited geometrical coverage were cca 30%.
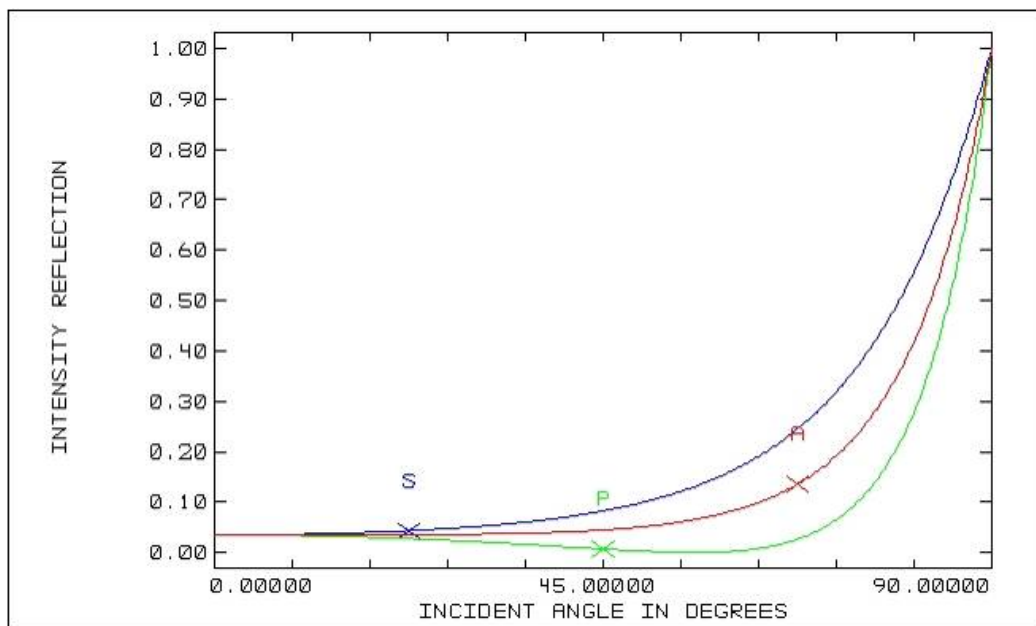
Figure 3.3*: Incident angle dependence of the reflectivity for the fused silica material at 550nm. Red and blue curves are for different polarizations, while the red one is for the unpolarized light.*

It was also found, that the Sol-Gel technology wasn't stable enough for the production of such a complicated shape in large quantities. Nevertheless, the UV transmission of the material was quite good and according to the producer the isotropy should be nearly ideal.

It doesn't seem reasonable to concentrate all the light by just one refractive surface in this case. No ray tracing simulations were needed thanks to the tests of the prototypes.
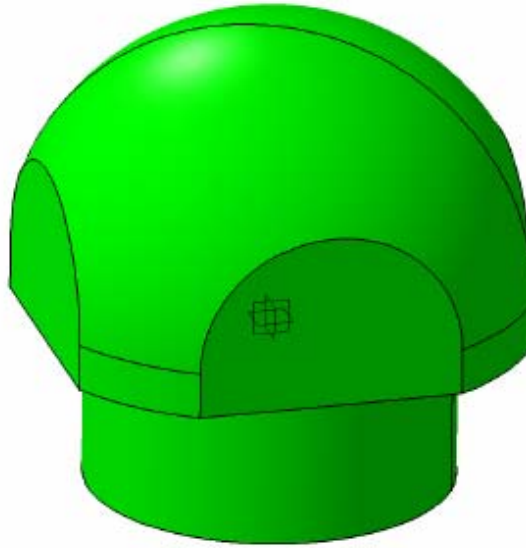
Figure 3.4: *"Mushroom" type silica lens produced by the Sol-Gel Novara technology. From [5].*

3.3.2 Hollow waveguide

The waveguide consists of a grid of reflecting surfaces transforming the entrance window's granularity to the corresponding pixels of the MAPMT, thus having a positive demagnification.
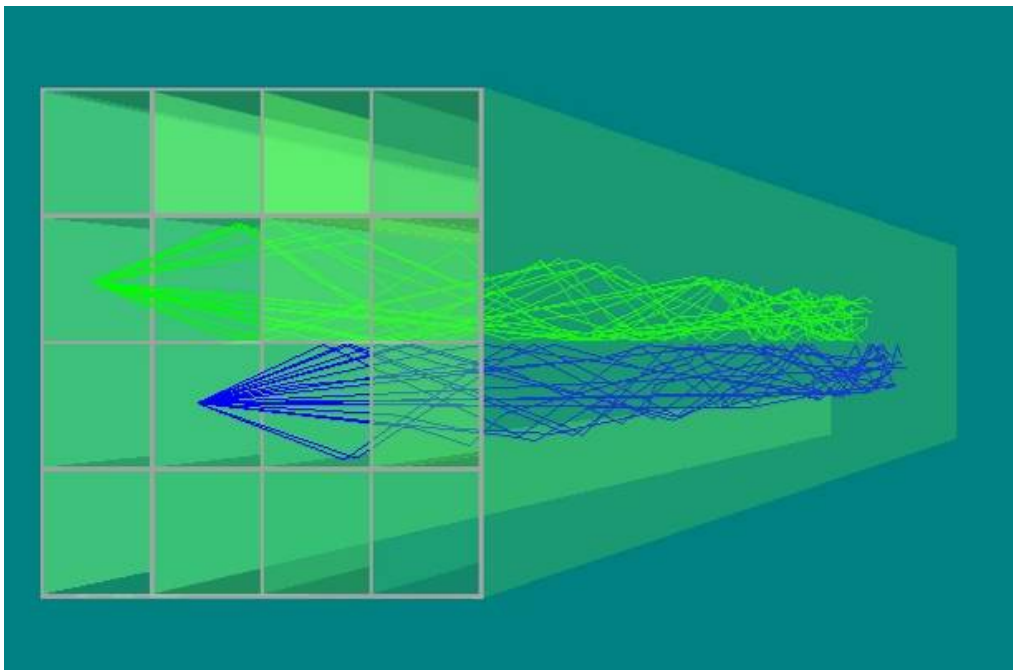
Figure 3.5: *Straight hollow waveguide with transmission simulated by two point type sources. MAPMT active surface is the more distant plane.*

To reach a minimum dead space in the entrance window, one should use relatively thin walls with a deposited reflective layer. On the other hand, the walls of cca 0.4mm would cover the spaces between the anodes (0.3mm) thus decreasing the crosstalks of the MAPMT. The waveguide can be produced for example by gluing very thin (even 0.05mm) glass plates or by injection molding.

The molding material should have a very low viscosity because of the complicated shape and the necessity to inject material only through the thin wall edges. It should be also appropriate for galvanic or vapor deposition of reflective layers. Such material is for instance ABS GP35.

One could use a steel or hardened silicon negative mold. The steel mold is really long-lasting and suited for large production sets (millions of pieces) but is very expensive. On the other hand, the progressive hardened silicon technology is used rather as a rapid prototyping method, but one could imagine a production of cca 600 pieces.

It was found, after several contacts with industry that one can not mold in practice the waveguide in one piece. The unfolding of the mold in 13 different directions would be quite difficult, but one could think about the production of the inner frame and the outer shell separately.

The major problem of this approach is the dependence of the phase space acceptance on the system length. One can easily derive the equation for the limit number of reflections n_{max} when a ray starts to travel back towards the source:

$$n_{max} = \frac{90 - \theta_0}{\alpha} \qquad (3.1)$$

with θ_0 the angle between the original incident ray and the detector plane normal (12.5° in *Fig. 3.4*) and α the angle between the reflecting surface and the detector plane normal (3.7° in *Fig. 3.4*). The formula is valid for the central part of the waveguide and for only one plane.
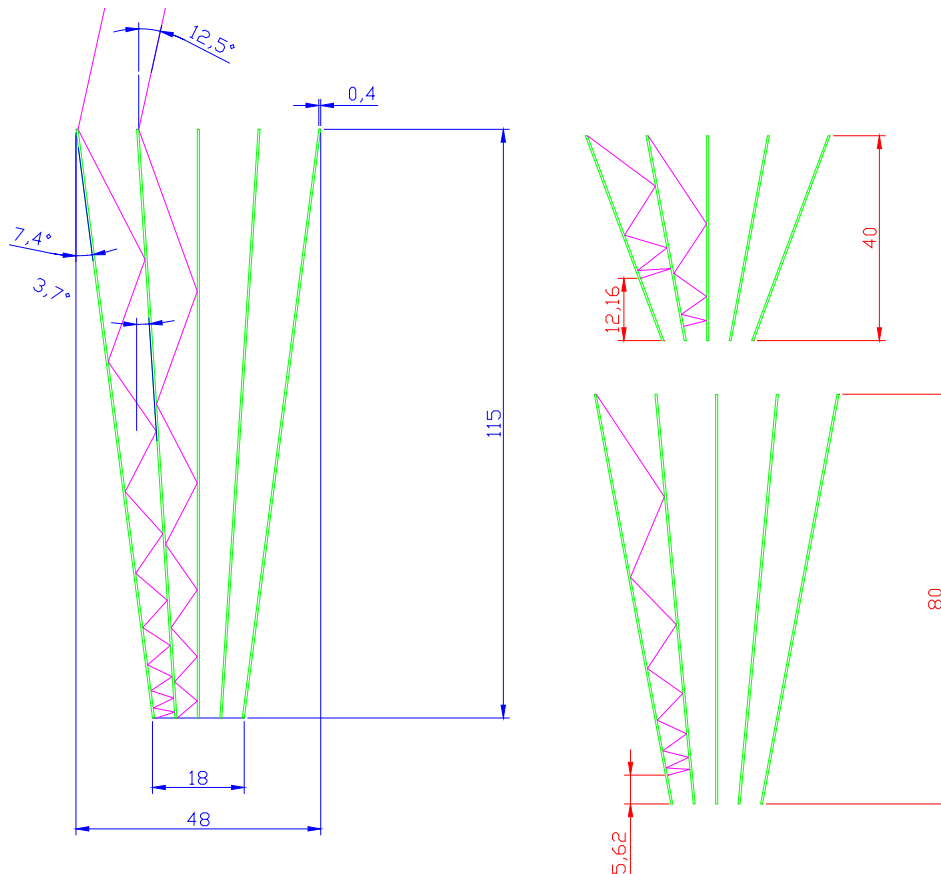
Figure 3.6: *Acceptance study for cross sections of hollow waveguides with different lengths. The designs on the right can not transmit the incoming (violet) ray. Units are millimeters.*

It is more convenient to make a direct study with consecutive reflections as shown on the Fig. 3.4. For the angular acceptance of 12.5° one would need the system length of at least 115mm. In such case, the waveguide could be mounted as a straight system with its main axis at 11.3° and the angular acceptance would match the required minimum range from the Fig. 3.2.

There was a small prototype produced by a rapid prototyping method (deposition of a thin melted plastic wire) to check the possibility of producing thin 0.5mm walls and eventual use as positive mold for the silicon technology.

Figure 3.7: *Photo of the plastic prototype of a hollow waveguide. The system length was cca 30mm. The fine structure is caused by the rapid prototyping method.*

The prototype clearly demonstrated the possibility of production of such geometry, but the surface quality was very poor and thus not usable as a mold.

3.3.3   Fused silica waveguide

The concept of a fused silica waveguide is more interesting from the point of view of production simplicity and increased angular acceptance. Thanks to the index of refraction of about 1.47, the incident angle of 12.5° transforms to 8.5° according to the Snell law [9]. The reflective walls would have to be covered by a reflective layer, because the total internal reflection seriously limits the acceptance. The geometrical shape is almost identical as the hollow waveguide, just instead of air it would be filled with polished ingots of fused silica.

The major problem with this design lies between the exit surface of the waveguide and the entrance window of the MAPMT, where is inevitably an air space. To avoid the total internal reflection of higher angle rays, one would have to use some index of refraction matching glue. No such glue transparent in the required UV range was found.

The price of material would be also a seriously limiting problem for this approach.

3.3.4 Telescope with 2 lenses

This is a very promising design, because its functionality was proved in the HERA B RICH detector [6].
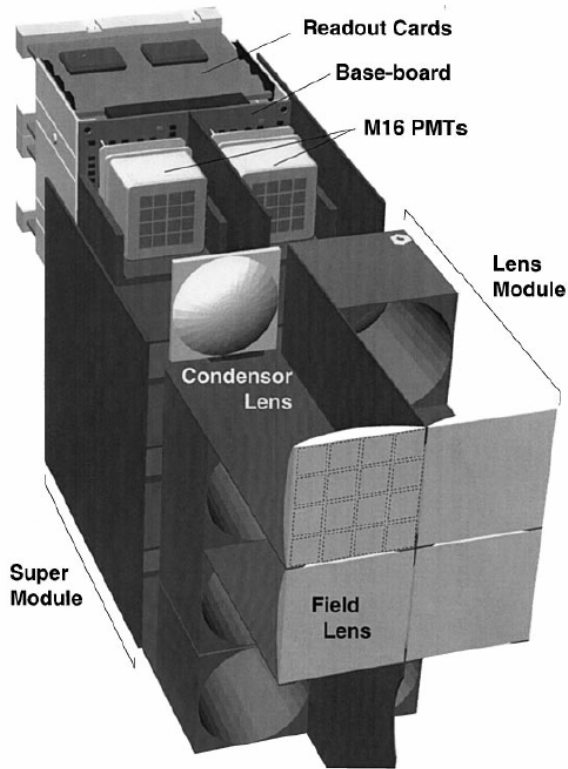
Figure 3.8: *Schematic of the HERA B RICH photon detector. From [6].*

The concept consists of a field lens placed in the focal plane of the mirrors (where the rings are formed) and a condensor lens between the field lens and the MAPMT. The front lens is used to bend the rays not passing through the center of the lens towards the condensor lens thus increasing the field of view of the system. In the first approximation, the condensor lens defines the magnification of the telescope.

The HERA B system was using injection molded aspheric acrylic lenses with extended transmission in the near UV (cutting edge at 300nm). It was designed for a demagnification of 2:1 and with an aperture cutoff at 140mrad (8°).

3.3.5 Telescope with 2 Fresnel lenses

Fresnel lenses can be a good choice for designs, where the system mass and lens thickness is critical and the optical material can be UV transparent plastic.

During the specification period of the concentrator optics, several types of the MAPMTs were considered, therefore the quantum efficiency wasn't known exactly. The chosen type had such QE, that plastic material transparent in UV (down to 300 nm) could

be used. But later, Hamamatsu further increased the transparency of the entrance window down to 200 nm. In that case even 1mm of the plastic would have nearly 0% transparency, so this approach wasn't investigated after the announcement from Hamamatsu.

3.3.6 Design concept choice

The different possible designs were discussed during a RICH1 working group meeting. The concept of a thick lens was rejected because of its low collecting efficiency and optical quality. No solution was found for the missing UV transparent glue necessary for the fused silica waveguide. The hollow waveguide seemed promising, but many remaining questions about production feasibility or possible coating quality could be a serious problem for the very tight timescale of the upgrade project. Such concept would need more development time; otherwise one could risk unexpected complications.

Mainly for the proven reliability, the aspherical telescope was chosen as the main design concept.

The designing procedure should start by the best reachable imaging quality systems regardless of price and mechanics. Then one should gradually converge to an optimal design fulfilling all the given requirements.

The choice of material was very easy because of the expected UV transmittance, material isotropy (due to the light polarization) and cost. The fused silica (SiO_2) material was chosen. The exact type (purity) will be discussed with producers. Important disadvantage of the fused silica telescope design is the impossibility to compensate for chromatic aberrations by choosing different optical materials.

At the beginning, the molding procedure was considered for the aspherical lenses production. Several producers were personally contacted, but it was found extremely difficult to mold the fused silica which has the softening temperature around 1600 °C, hence the standard glass molding techniques are not possible.

There are nevertheless several producers in Europe able to grind and polish aspherical optical surfaces at a reasonable cost with very sophisticated numerically controlled machines.

4 Telescope design

4.1 ZEMAX code introduction

Zemax program is an optical design and ray tracing computer code. It was widely used for this work to build the models of the telescope and the Cherenkov light, optimize and simulate the design performances and verify the system sensitivity to production errors.

The program can run in two main modes. The sequential (**SC**) mode is using the paraxial approximation (sin(x) ~ x) and matrix formalism for the ray tracing algorithm, so the program can perform the simulations very fast. This mode is necessary for the optimization phase and all major optical quantities can be calculated there. Any optical system is defined sequentially surface by surface by its type, radius of curvature, thickness, material and aperture. Nonstandard surfaces have specific operands. It is very important to properly define the system aperture and thus the light beam properties.

The non-sequential (**NSC**) mode is used primarily for Monte Carlo type simulations. One can define almost any geometrical shape, because it allows CAD import. Order of the inserted individual objects is not important, because the simulation algorithm traces each ray point by point. The light properties are defined by source objects and can vary from individual rays to large random sets of rays. Detection of the rays is performed via segmented detector objects. More about Zemax can be found in [9].

4.2 Čerenkov light source model in ZEMAX

One can not use the standard design approach by placing object in front of the first lens and defining the aperture stop inside the imaging system. This approach was nevertheless tested and the results were non consistent. The light beam with properties corresponding to the real situation inside the RICH has to be modeled by parallel rays (from infinity) and an ideal paraxial lens with focal length equal to its distance from the detector plane.

The vertex angle of the light beam cone is defined by paraxial lens's aperture and should correspond to the required angular acceptance of the system. But still, the system aperture has to be explicitly defined in Zemax, so one has to select "float by stop size" aperture and set the paraxial lens as the field stop.
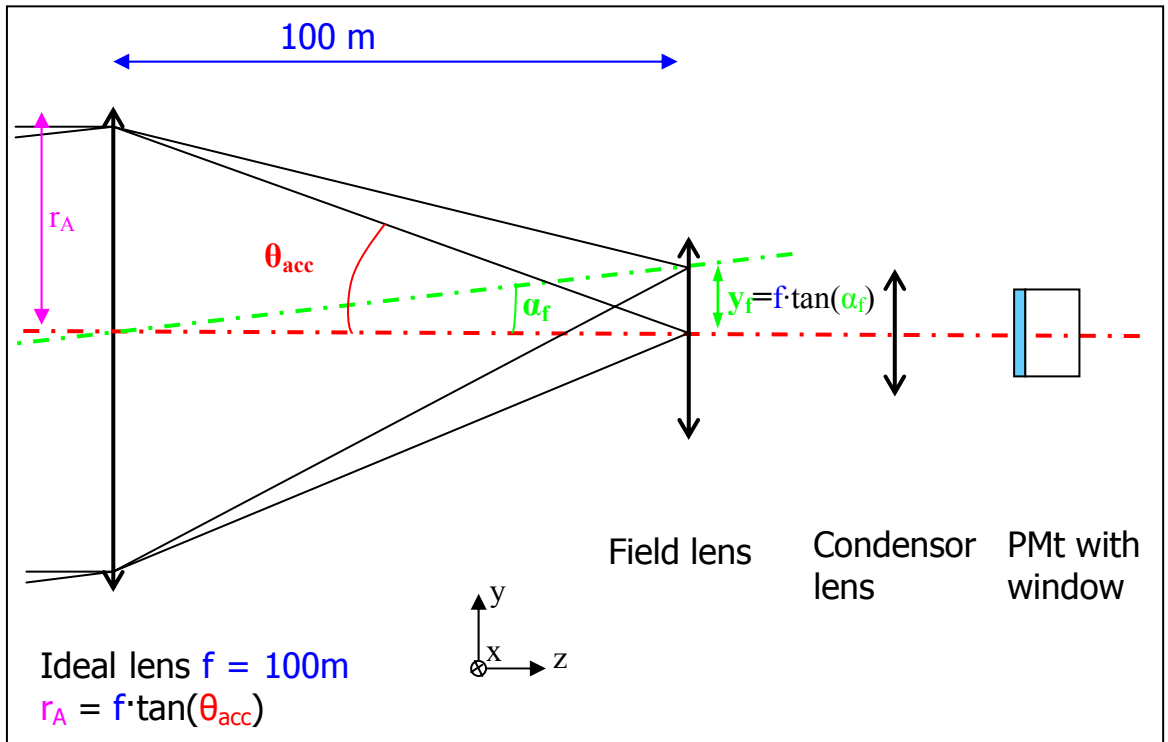
Figure 4.1: *Schematic of the light source definition by focalization of the rays coming from infinity by an ideal paraxial lens. System aperture stop is defined by the ideal lens.*

The field points (at y_f) are defined by inclination of the parallel rays as seen on Fig. 4.1. It is clear that y_f has to be smaller than the field lens physical dimensions. By defining various points, one can enable a balanced optimization for the whole clear aperture of the telescope.

It is important to select the correct wavelength range with corresponding weights (see Fig.3.2), which are used not only for the design optimization.

4.2.1 Aperture apodization

To allow a more accurate calculation of various optical parameters (for example the ideal point imaged spot size), one can use the pupil apodization.

It is just a weighted correction by the expected Gaussian distribution of the incident rays angle. Each ray at a normalized distance ρ from the center of the paraxial lens receives the weight A:

$$A(\rho) = e^{-G\rho^2} \qquad (4.1)$$

with G as the apodzation factor [9]. Assuming the standard deviation of 3.3° and the angular acceptance of 7.1° one gets $G = 2.35$. This setting was used even for larger acceptances, thus slightly underestimating the design performances.

Please notice that the system aperture is not modified by this effect.

4.2.2 Merit function for optimization

The merit function (**MF**) should contain properly defined imaging performances for different positions of the light cone and for the wavelengths weighted as on the Fig. 3.2. The MF is then the sum of squares of individual operands and will be minimized during optimization.

For our case, there is no evident reason to deliberately allow worst performance for example in the corners, so all the field positions should have the same (or similar) weights. It is also imperative to implement the right border conditions.

All lenses' central and edge thicknesses and air spaces were constrained by maximal and minimal values. The optimization will have to be done with circular aperture of the front lens; otherwise, even if defining the minimum lens edge length, one would get mostly non-physical results. The square aperture has anyway the impact only on the vignetting of extreme field rays like in Fig. 4.6.

For the axial systems, the paraxial image height operand was used to reach the required magnification for the field lens diagonal. The geometrical distortion was also constrained to a reasonable level.

For the overall imaging quality targeted to the RMS spot size, the powerful default merit function was generated for each wavelength and field position.

The optimization can run in three different modes. The standard mode searches the local minimum of the MF. The convergence speed strongly depends on the design type, number of degrees of freedom, complexity of the merit operands, "distance" from the minimum etc. Once the minimum is found, it is reasonable to run the Hammer optimization, which tries to start the procedure with slightly different initial conditions and thus escape the local minimum. The last mode is the Global optimization searching the minimum in the whole parameter space allowed by the MF. In this case, the limiting conditions have to be set very carefully and then the program can be running for several hours or days on a single CPU machine.

A special care should be given to the initial design parameters so that it doesn't exhibit total internal reflection (**TIR**) for any field or wavelength. The MF calculation would be

impossible in this case or the optimization procedure would fail very soon (if very close to TIR).

The default part of the MF was found adequate for our problem and any additional aberrations except the geometrical distortion were not explicitly added.

The MF for non-axial designs has to be more complicated. When the design stops to be axial, the paraxial operands in the Zemax merit function have no meaning anymore. Mainly the paraxial image height and the geometrical distortion operands can't be used.

This problem was solved by using the operand CENX and CENY, which means image centroid position in the given axis projection. The centroid is determined by lunching many rays through the corresponding field lens position (imaging an ideal point) and calculating the geometrical center of the resulting spot. In such a way, the image height can be set in different image locations according to the needs and it has a direct impact on the geometrical distortion, which is caused by variation in magnification for different fields.

The magnification was set by using differences between positive and negative x and y centroid positions of the corner and edge field positions. The central field centroid position was maintained near the PMT center. In the later designs, the system length was also constrained (or minimized).

4.3 Axial systems

The design phase begun by creation of axial systems with rather good optical parameters regardless of the incident light axis and system cost.

4.3.1 HERA-B design

A short study was made to reconstruct and see the performances of the HERA B RICH photon detector design.

The aspherical surfaces of the system were defined by the following formula:

$$z = \pm \frac{\rho^2}{2R_i}\left[1 + \frac{b_i}{4}\left(\frac{\rho}{R_i}\right)^2\right] \qquad (4.2)$$

with b_i as the dimensionless aspherical coefficient of 4th order, ρ the radial distance from center, R_i the nominal surface radius and z the surface coordinate (parallel with lens axis).

This equation can be easily compared with the equivalent formula used by Zemax for the even aspheric surface:

$$z = \frac{\dfrac{1}{R}r^2}{1 + \sqrt{1 - (1+k)\dfrac{1}{R^2}r^2}} + \alpha_1 r^2 + \alpha_2 r^4 + \alpha_3 r^6 \dots \qquad (4.3)$$

where the aspheric coefficients α_i have dimensions according to their order and k is a conical constant (null for all our cases). The first spherical term from Eq.4.3 translates after a small approximation into $\dfrac{r^2}{2R}$, so it is equivalent with Eq.4.2. Thus the 4th order coefficient α_2 can be written as:

$$\alpha_2 = \frac{b_i}{8R^2} \qquad (4.4)$$

After this transformation, the design was reproduced in the Zemax code.
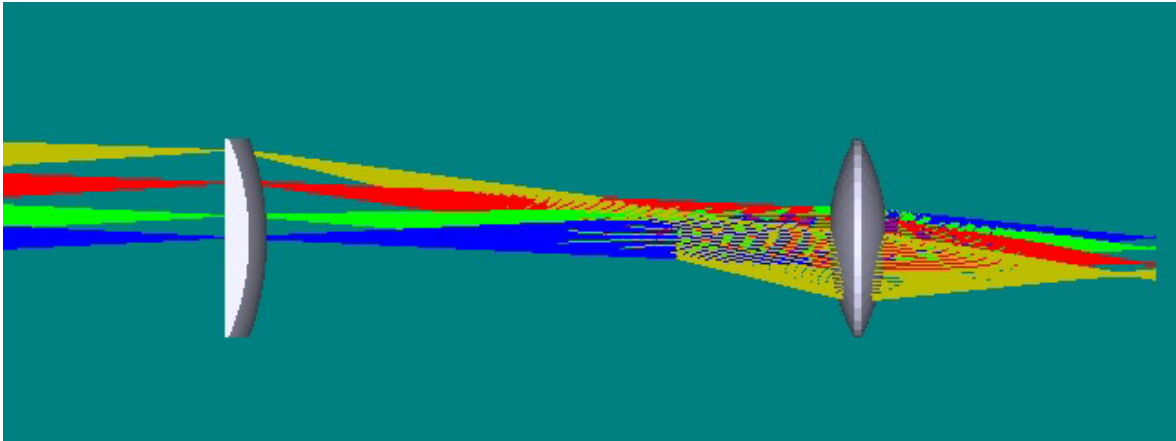
Figure 4.2: *Schematic of the HERA B RICH concentrator aspherical optics with light cones modeled in different field lens's locations (in diagonal plane).*

The design performance was studied in the wavelength range 380-500nm and at different incident cone vertex angles.

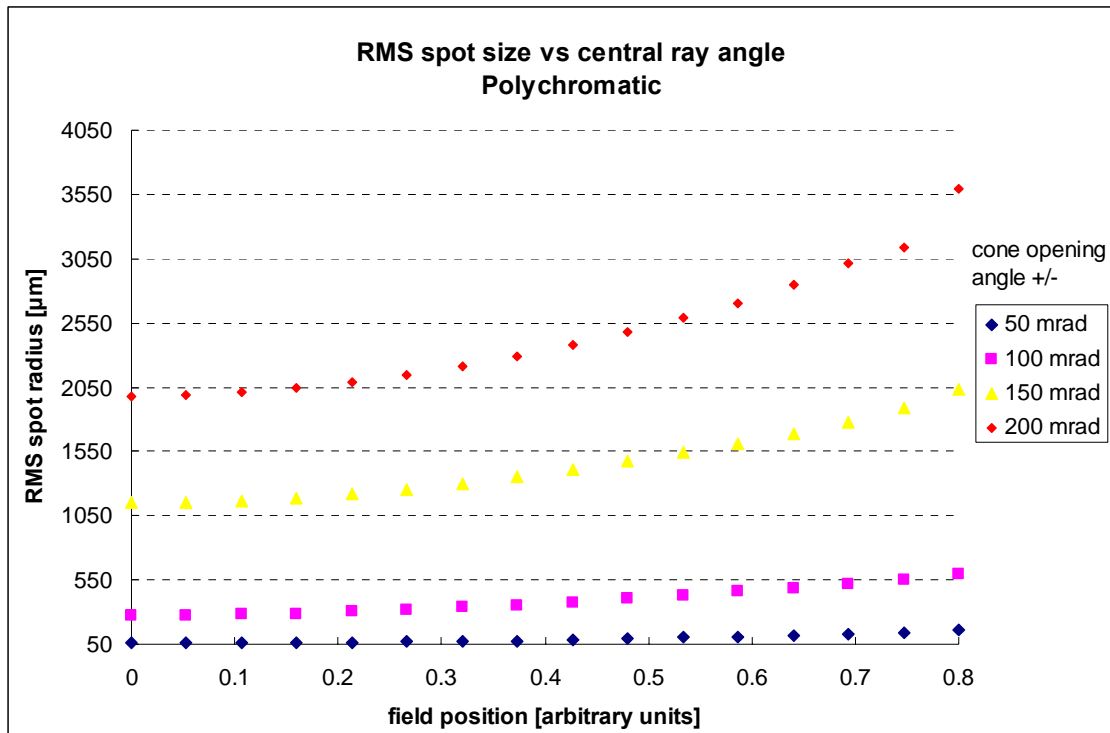**Figure 4.3:** *Simulated polychromatic imaged spot size radius vs. incident light position on the field lens surface (0.8 corresponds to the lens corner) for different cone vertex angles.*

From the Fig. 4.3, one can see the rapid increase of the RMS spot size for higher light cone opening angles. The presented data are averaged for different wavelengths, similar plot for individual wavelengths can be found in attachments Fig.10.1. Monochromatic geometrical (barrel) distortion of the design can be qualitatively evaluated from the Fig. 4.4, where one can also see the magnification ratio 2:1. The quantitative estimation is on the Fig.10.2 in the attachments.
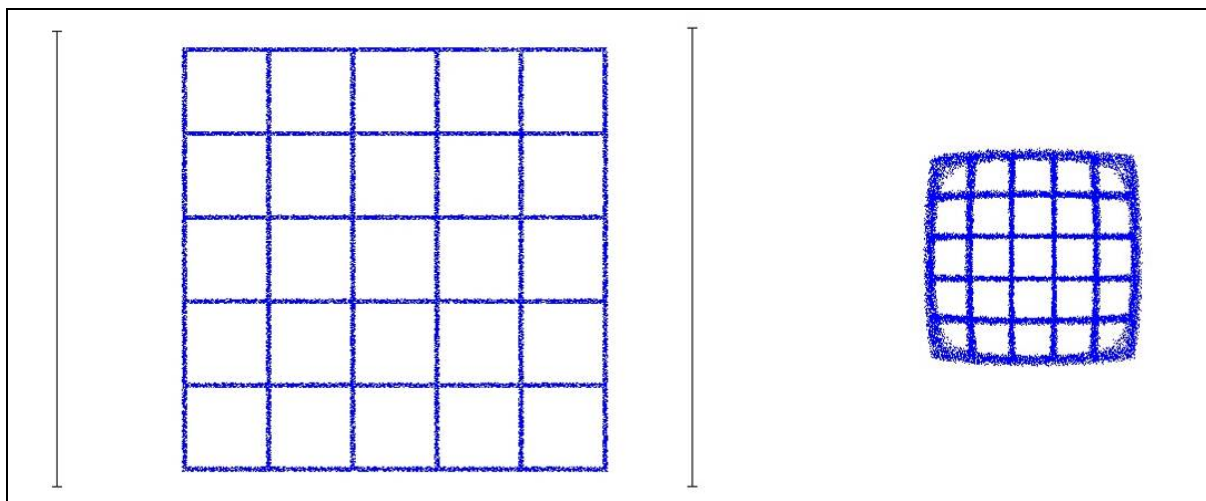
Figure 4.4: *Ideal grid projected to the mirrors focal plane (left) and its simulated image on the photocathode. The resulting geometrical distortion is 10.4% in the corners.*

4.3.2 Starting point for optimization

For a successful optimization one needs a good starting point design having a reasonable performance and a well built merit function mathematically describing the performances and requirements.

As the first design attempt, the reproduced HERA B system was used. The correct magnification target was placed in the merit function together with an automatically generated function targeted to the RMS spot size for the defined field positions. The light source had to be modified to enable the magnification operand. All dimensional parameters were optimized and the object position was located just in front of the field lens and the system aperture defined by incident light cone angle.

This approach failed because of the light source definition, which forces the light beam to pass through the center of the condensor lens (defined as field stop). Thus the light (at the source level) near the lens corners is more inclined towards the lens axis than in the center. This led to an optimized design but for a very different case.
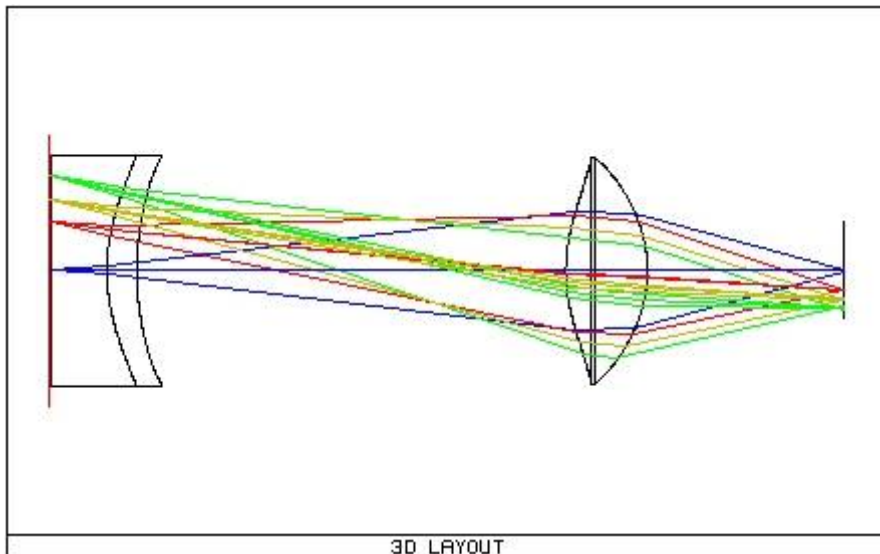

Figure 4.5: *Incorrectly optimized design cross section derived from the HERA B system.*

It is clear despite the good imaging performances (see Fig.10.3 in attachments), that the negative field lens is decreasing the field of view and the optimization procedure has to be changed.

4.3.3 Axial case results

Several axial systems were designed with different angular acceptances, number of aspherical surfaces and imaging qualities. Only the standard optical parameters such as the geometrical distortion or spot size were checked in this stage. Even if they do not have the direct impact on the detectors specific imaging performance, they can be a valuable indication of the design's quality.
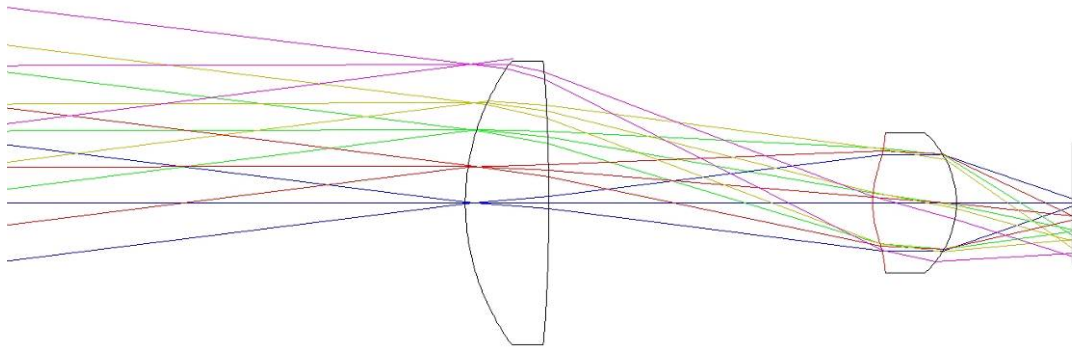
Figure 4.6: *Axial system with correct magnification, 1 aspheric surface and light beam definition with paraxial lens at 10 m distance creating a small field curvature.*

Better performance evaluation is described later in chapter 5.

The optimization procedure might have been slightly influenced by the field curvature (Fig.4.6) caused by the 10 m long distance from the paraxial lens. This length was then increased to 100 m and the curvature was then negligible.
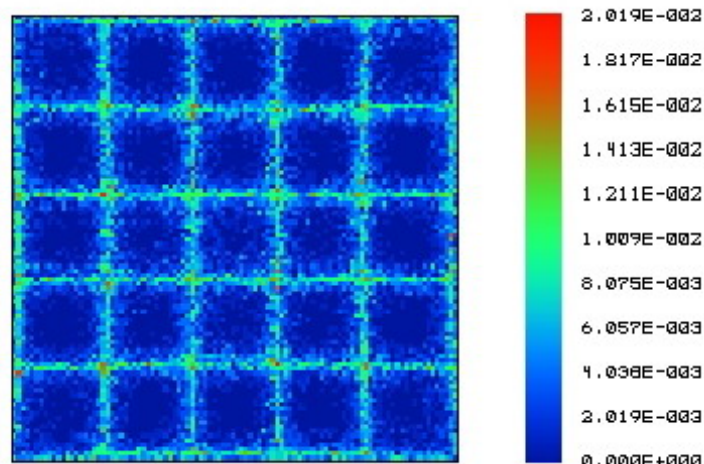
Figure 4.7: *Polychromatic regular grid imaged by the system from Fig.4.8 plotted in false colors. The units are watts/cm² and the square side is 18 mm.*

The first designs had a limited angular acceptance to guarantee the optimization stability, but it was gradually increased from 6 to 7.1 and 8.3°. The acceptance of 9° was

also reached, but the result was very poor. At the beginning, as the system was derived from the HERA B design, all the surfaces were optimized with their 4th order aspherical coefficients. The coefficients were progressively removed and even the fully spherical case was investigated but with a poor result. All the later produced aspherical designs contained only the fourth order coefficient to ensure the feasibility of the lenses.
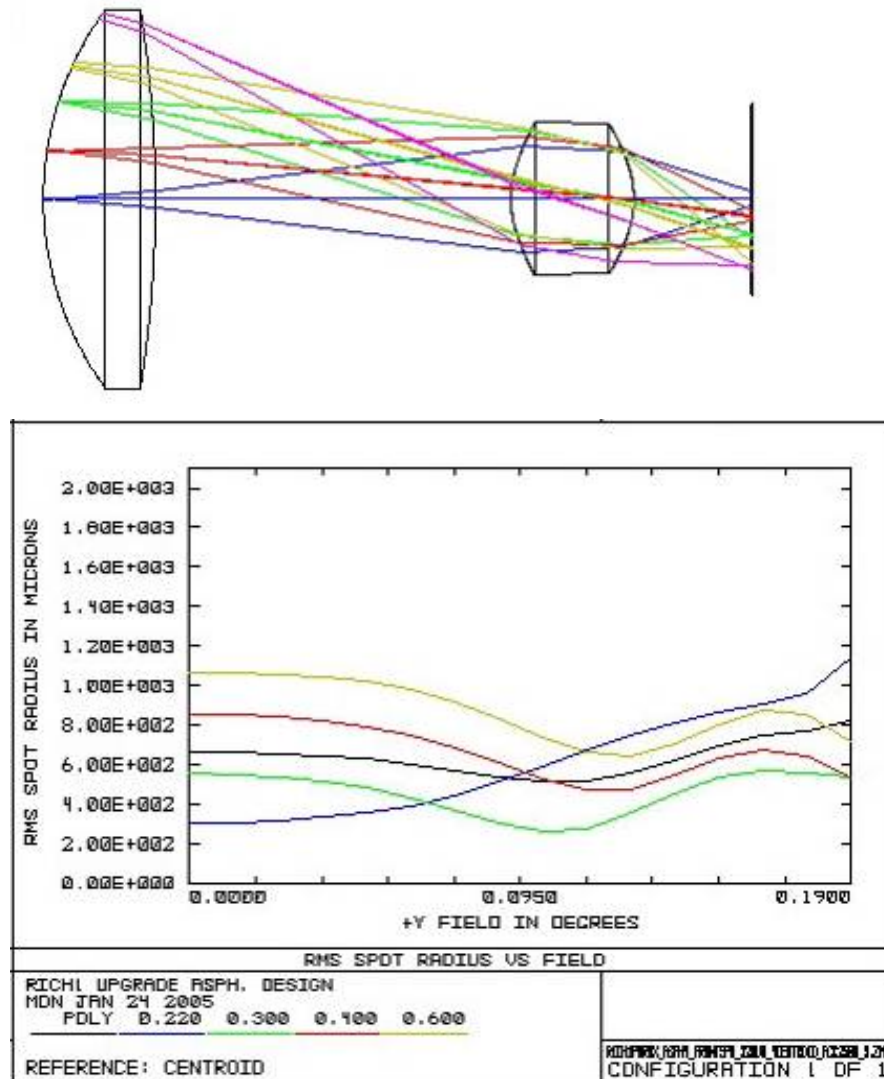
Figure 4.8: *Example of axial design with angular acceptance of ±.7.1°, the front lens is fully spherical. The black polychromatic line (imaged spot radius) is the weighted sum for the basic wavelengths. The +Y field of 0.19° corresponds to the field lens corner.*

It is important to underline, that the ray colors from the top part of the Fig.4.7 are not related with the ones in the RMS spot size plot. The top ones represent different field positions. The Fig.4.8 is supplied for comparison with the HERA B design geometrical distortion (Fig.4.4). The distortion is in the form of a pincushion this time.

4.4 Non - Axial systems

It was found rather unfeasible to build a simple two lens telescope with the required angular acceptance of ±11.3° from the system axis (see Fig.3.4) and a reasonable performance for all the field positions. The next step is rationally some kind of a non-axial solution.

4.4.1 Simply tilted system

The basic idea of this approach is to keep the front field lens's axis parallel with the mean axis of the incident Čerenkov light. The required space should be then obtained by tilting the condensor lens together with the image plane on the photomultiplier.

The lever arm of the tilt would be quite short in this case (condensor lens thickness plus its distance to the MAPMT photocathode), but it was necessary to investigate the possible extent of such tilt.

Another possibility is to leave the front lens at 11.3° tilt, thus at 4.7° (Fig.4.9) from the mean light axis and try to tilt and off-center the second lens and move also the PMT. This would result in a system with three different element axes.
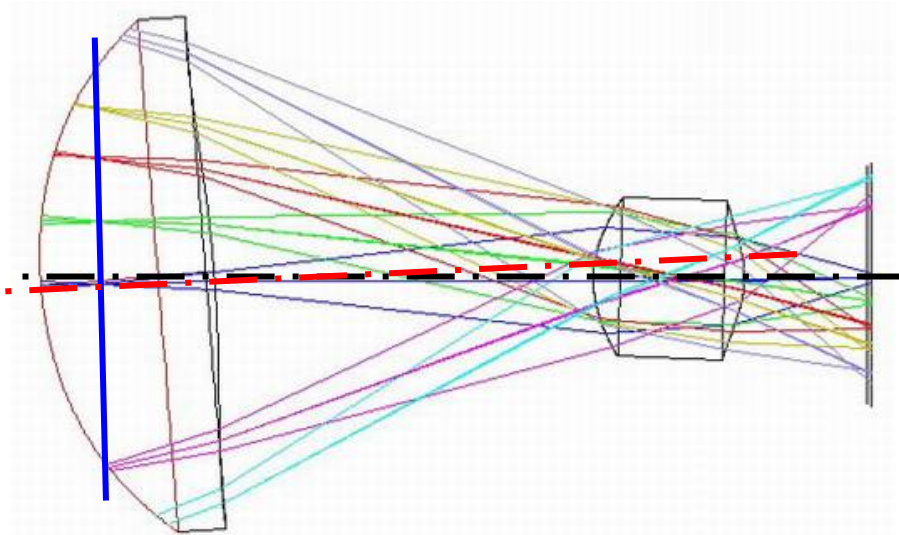
Figure 4.9: Non-axial aspherical system with 3 different axes. Front lens axis (red) lies at 11.3° from the detector plane normal. PMT window's axis (black) defines the horizontal plane for the plot (at cca 15.5°) and focal plane of the mirrors is in blue (thick line).

The simply tilted non-axial system can not solve our space requirements problems, as one can clearly see from the Fig.4.9. The allowed movements of the condensor lens are very limited and yet it has to be moved in the 'wrong' direction. The tilt and off-center of

the PMT can't recover for such movement. The ideal case for us would match the black and red axis on the Fig.4.9.

The results for the case with field lens placed at 16° with the condensor lens placed on the axis of the first lens were very similar therefore not providing more than 1 mm of extra space at the level of the PMT window.

4.4.2 Prismatic lens conception

The idea of a prismatic lens is basically very simple. It is necessary to bend the light rays in the vertical plane, so a prism can be 'inserted into' the field lens, hence creating a rotationally nonsymmetrical lens with different thicknesses along the vertical direction. The effects of the lens and the prism would then combine and allow the design to be non-axial.

During the proposal part of the telescope design, it was planned to produce the lenses by the molding procedure from the fused silica. The aspherical mold itself would represent the major cost for the production and any other serious complication like the aspherical prismatic lens would have been very problematic. With the possibility to produce aspherical lenses by numerically controlled grinding and polishing methods, this option became more realistic and started to be investigated during a telescope workshop in Trieste.

It was found for some designs that the field lens's second surface was close to infinite curvature. For one of these designs that surface was made flat and together with the spherical front surface of the field lens was used in all the designed prismatic systems.

4.4.3 Possible design variations

Several similar systems were designed and later simulated to select an optimum solution for the telescope with the prismatic field lens. The differences were mostly in the angular acceptance and the number of aspherical surfaces.

The prismatic form was implemented by tilting the flat surface of the field lens along its horizontal axis. The tilt was fixed after several attempts to the reasonable 5°.
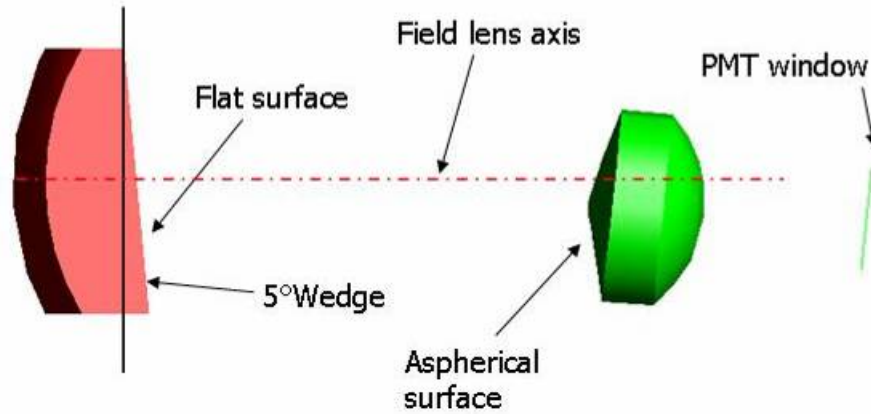
Figure 4.10: *Horizontal projection of a non-axial system with the prismatic field lens and 1 aspherical surface on the condensor lens. Red axis is parallel to the mean light direction.*

The four designed system's basic dimensions are summarized in the Table 4.1. The tilt of the condensor lens was targeted to at least 5.5°, but the optimization didn't reach this requirement exactly for all the designs. The second lens is tilted vertically around its front vertex, therefore it was necessary to add a vertical displacement to follow the light path (last column in Tab.4.1). The MAPMT window's axis is parallel with the second lens's axis but it has to be moved back by 1.5 mm to keep the image center in the middle of the photocathode.

Design	Acceptance ± [°]	Aspheric surfaces count	Condensor tilt [°]	Condensor/PMT off-center [mm]	System length [mm]
A	7.1	0	5.50	-3.6/+1.5	148.9
B	7.1	1	5.48	-3.6/+1.5	145.6
C	8.3	2	5.40	-4/+1.5	149.4
D	8.3	1	5.46	-4/+1.5	143.7

Table 4.1: *Summary of the main dimensions of the designs with prismatic field lens. The later chosen design is in the green frame.*

The imaging qualities' differences depend mostly on the varying number of aspherical surfaces and different surface curvatures; all the condensor tilts can be approximated to 5.5°, thanks to their lower impact. The light beam used for calculating for example the RMS spot size is copying the acceptance, so the results for the design B should be theoretically better than for the case of D. The fully spherical design A was investigated to check the possibility of producing a relatively cheap design without any aspherical parts. The design C with fully aspherical condensor lens is meant to be compared with D, but its production price would be too high in fact.

Design	A	B	C	D
$10^5 \cdot \alpha_{2F}$ [m^{-3}]	0	-5.1742	-3.8844	-6.13884
$10^5 \cdot \alpha_{2B}$ [m^{-3}]	0	0	1.0745	0
R_1[mm]	55.646	52.272	54.906	54.937
R_3[mm]	23.278	23.194	24.011	20.696
R_4[mm]	-27.803	-21.834	-23.219	-24.964
T_1[mm]	16.419	20.504	21.040	20.813
T_2[mm]	83.675	77.567	79.264	75.805
T_3[mm]	20.487	18.529	20.086	19.420
T_4[mm]	27.782	28.467	28.501	26.835
D_3[mm]	33.38	35.35	36.63	34.68
DIST[%]	14.3	10.8	12.5	13.5

Table 4.2: *Summary of the construction parameters and performance data for the designs with prismatic field lens. The later chosen design is in the green frame.*

The Tab.4.2 summarizes the important lens's construction parameters. The aspherical 4th order coefficients (Eq.4.3) for the front and back side of the condensor lens are on the first two lines. They are followed by radiuses of curvature *R* of the optical surfaces and by the surface thicknesses *T* or lens distances. Before the maximum geometrical distortion at 300 nm (image corner), there is also the diameter *D* of the condensor lens. The convention for the transformation operation is: first decenter then tilt as it is visible on the Fig.4.11.
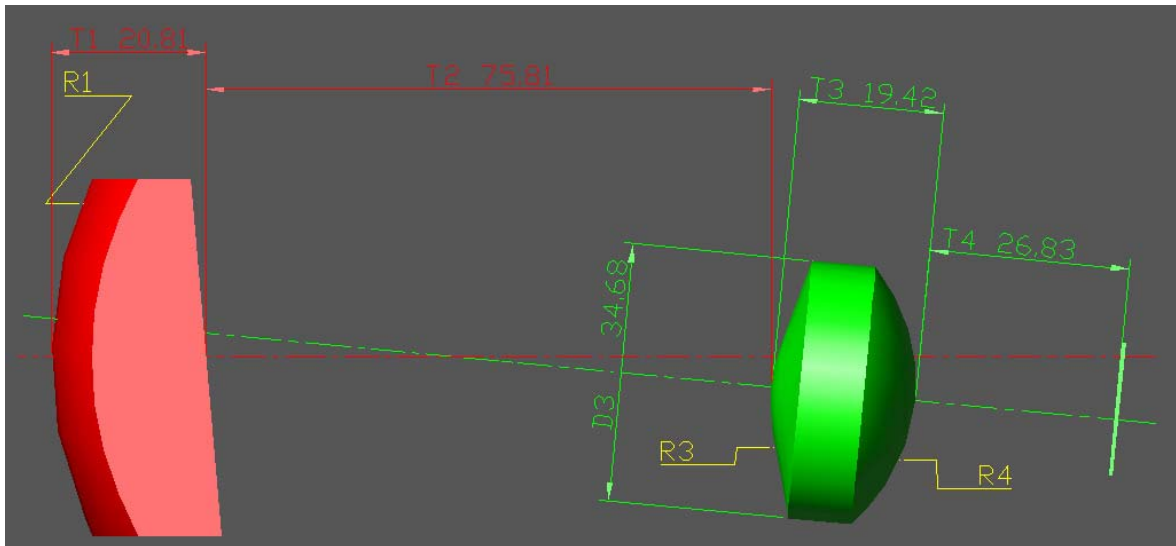
Figure 4.11: *Non-axial design D with dimensions definitions as used in Tab.4.2.*

The red dimensions are aligned with the red field lens's axis, because the decenter is used prior the tilt. The green axis belongs to the condensor lens obviously. The surface curvature is the basic radius *R* from the Eq.4.11 also if the surface is aspherical.
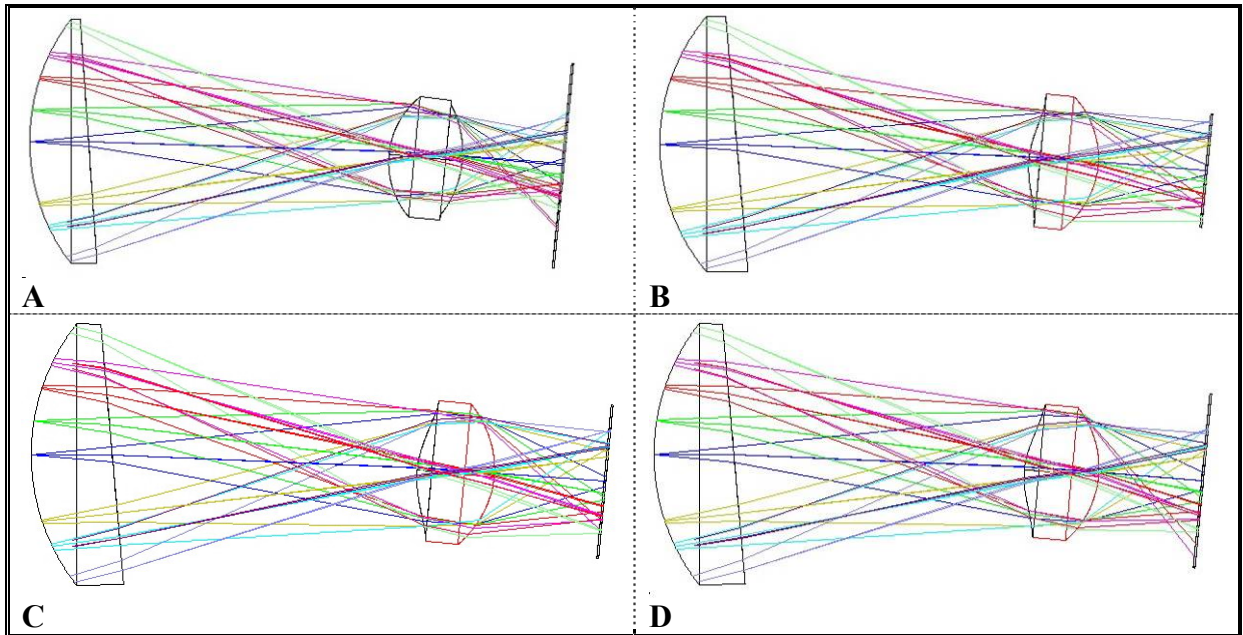
Figure 4.12: *Cross sections (with rays from several field positions) of possible variations of the design with prismatic field lens.*

Individual design reports for the designs A, B, C and D can be found in the attachments. The reports contain a simulated image of an ideal grid showed in false colors (as it was previously used in the Fig.4.7), design cross section with different rays, RMS spot size plot and geometrical grid distortion. The distortion plot contains a regular grid as it (grid nodes) would be imaged by the rays almost parallel to the field lens's axis. The crosses are the corresponding centroid positions traced by means of the full acceptance light beam. The maximum deviation between the two matching points relative to the distance from the image center is also written in the last line of the Tab.4.2.

It was later proven by the person responsible for the mechanical housing that such types of non-axial setup fulfill our space requirements and can be mounted into the 12 by 12 array.

5 Performance simulations

The problem specific imaging performance of the telescope design can not be simply expressed by the basic optical parameters such as the geometrical distortion or the spot size. Sets of simple ray tracing simulations were proposed instead.

## 5.1 Source files for Monte Carlo simulations

The basic idea for the performance tests is to target by a set of rays the field lens surface, which should be imaged to the corresponding pixel in the MAPMT and compare the number of rays or their energy collected by the right pixel with the rays, which strike other pixels or get lost elsewhere.

NSC mode of ZEMAX has a built in support for Monte Carlo (**MC**) type simulations. Once the system's geometrical shape and materials are defined, one has to place correctly the detector surface and the light ray(s) source.

Most of the predefined sources have some kind of a random generator producing diverse beam shapes and distributions, but none of them was found suitable for direct integration into the required model. It was decided to provide a simple external ray generator.

A Matlab script was generating rays with uniform random distribution of the stating position inside a given rectangle in the transverse plane; mostly a square of 12x12 mm corresponding to 1/16 of the area covered by one field lens. Each ray was also defined by three directional cosines. The angle from the longitudinal axis had a normal random distribution with $\sigma = 3.3°$ (without any cut for the angles), as it was previously defined in the specifications. The remaining cosines were turning the ray around the longitudinal axis to produce a uniform distribution of direction in the transverse projection. The last entry generated for each ray was the relative energy, which was set to *1/N*, with *N* as the number of rays in the produced file with '.dat' extension.

The short script can be found in the attachments (Fig.10.8).
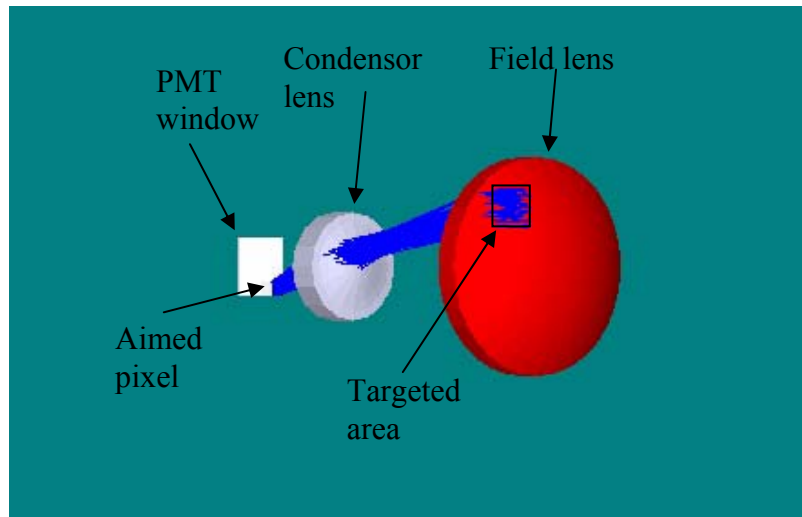
Figure 5.1: *Example of a MC simulation – targeting a corner of the field lens by a set of rays generated via Matlab script.*

It is clear from the Fig.5.1 that all the telescope designs are inversing the image, so the image reconstruction software and hardware will have to account with this little complication. But the optical system shouldn't complicate the data acquisition any further thanks to the basic target of the design, which is the imaging independence on the incident ray angle. If a photon from the Čerenkov ring hits the field lens (with incident angle within the given acceptance), it is imaged on the corresponding opposite pixel and no further information about the angle is needed for correct reconstruction of the ring position in the mirror's focal plane.

There was another similar type of source file produced later. All the rays had the same direction and filled the whole field lens's area. Its use is described in the chapter 5.3.

During the telescope design workshop in Trieste, yet another source file was provided by Andreas Mutter by transforming the data from a complex MC simulation of the COMPASS detector.

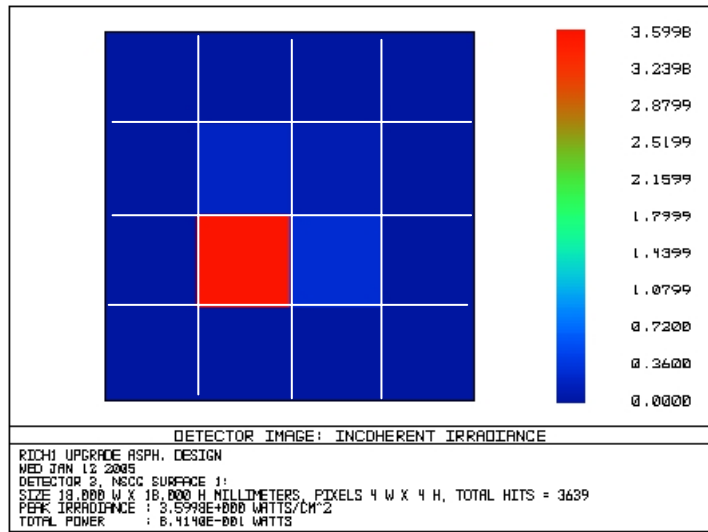## 5.2 Non-axial designs comparisons

To compare the imaging performances of different designs, the following procedure was used.

The mirrors' focal plane in front of the field lens was virtually divided into 16 identical pixels. A set of rays from the source file covering the same area as the pixel was placed in

one of the 16 locations in the focal plane in such a way to hit the corresponding pixel on the photocathode from the Tab.5.1. The rays were then traced through the system.

MAPMT Pixels mapping			
		E	D
		G	F
C	A		
B	H		

Figure 5.2: *Mapping used in performance simulations.*

DETECTOR IMAGE: INCOHERENT IRRADIANCE
RICH1 UPGRADE ASPH. DESIGN
WED JAN 12 2005
DETECTOR 3, NSCC SURFACE 1:
SIZE 18.000 W X 18.000 H MILLIMETERS, PIXELS 4 W X 4 H, TOTAL HITS = 3639
PEAK IRRADIANCE : 3.5998E+000 WATTS/CM^2
TOTAL POWER : 8.4140E-001 WATTS

Figure 5.3: *Result of a simulation using 10k rays.*

Each simulation was using 10^4 rays with colors randomly attributed with respect to the predefined weights. The detector with 4x4 pixels was placed inside the MAPMT entrance window to simulate the photocathode deposited on the back side of the window. The total energy transported by the rays was always 1 W and all the rays had the same fraction of energy and random polarization.

Two types of simulations were performed for each pixel position mostly to crosscheck the results. The first one was just a simple ray tracing through the lenses and the window up to the detector. The total number of hits on the detector's sensitive area (18x18 mm^2) was recorded together with the peak irradiance in W/cm^2 corresponding to the energy deposited on the aimed pixel.

The subsequent simulation was counting for polarization effects and using a ray splitting procedure, where every ray striking a boundary between two media splits in two rays. One is reflected and the second transmitted and both have energy related to the reflectance (and transmittance) of the surface, which depends upon the difference of the refraction indices and the angle of incidence (see Fig.3.3). The splitting procedure is stopped when the ray has its energy lower than a fixed threshold or escapes from the design area. The total energy collected by the MAPMT's sensitive area and the peak irradiance was recorded.

An example of the result of such simulation using ray splitting is shown on the Fig.5.3, where the pixel A was aimed.

The procedure was done consecutively for all the pixels from the Fig.5.2 for the non-axial designs. For the case of axial systems, only four pixels were tested to take advantage of their axial symmetry.

The problem specific figure of merit (FOM) [S. D. Torre, private communications] was built to compare the results of the simulations:

$$FOM = \frac{\sqrt{f}}{\sqrt{13 - 12f_p}} \qquad (5.1)$$

where f is the fraction of the generated energy collected by the detector and f_p the fraction of the collected energy concentrated on the correct pixel.

The formula should express the imaging performance related to the ring measurement error. The f comes from the standard deviation of the measured ring radius $\sigma \sim \dfrac{1}{\sqrt{N}}$ with N as the number of detected photons. Since we want to minimize the FOM and σ, f is in the nominator. The denominator relates on one side the standard deviation for the case, when f_p photons hit the correct pixel, what gives the single photon position uncertainty $\sigma \sim \dfrac{1}{\sqrt{12}}$ (due to the uniform sensitivity on the whole pixel). On the other side it considers the case when approximately $(1 - f_p)$ photons miss the right pixel and strike one of the neighboring pixels.

Design D	No ray splitting		With ray splitting					
Pixel	N/N_{det} [%]	E_{peak} [W/cm^2]	E/E_{det} [%]	E_{peak} [W/cm^2]		f	f_p	FOM
a	99.58	4.43	81.62	3.61		0.8162	0.9009	0.6105
b	97.51	4.25	79.60	3.48		0.7960	0.8826	0.5749
c	98.66	4.32	80.67	3.52		0.8067	0.8867	0.5847
d	90.01	4.11	73.56	3.36		0.7356	0.9246	0.6215
e	97.78	4.31	80.10	3.52		0.8010	0.8926	0.5916
f	98.02	4.34	80.19	3.54		0.8019	0.8966	0.5982
g	99.68	4.47	81.81	3.66		0.8181	0.9081	0.6237
h	99.15	4.23	81.24	3.45		0.8124	0.8639	0.5555
				Average		0.80	0.89	0.595

Table 5.1: *Example of data from one complete simulation of the design D.*

The fraction of energy f detected by the PMT is simply E/E_{det} from the simulation using ray splitting option, because the total energy used was always 1 W.

The f_p is calculated by:

$$f_p = \frac{f}{E_{peak} A_{pixel}} \qquad (5.2)$$

with A_{pixel} as the active area of the detector's pixel (0.2025 cm^2).

The simulations were used also for testing the previous designs and thanks to the results the centroid positions in the MF were changed to better balance the resolution in the central area and the losses in the corners.

The Tab.5.1 shows the resulting data from the simulations of the prismatic design D. The worst performances were usually in the corner pixels because of the highest pincushion distortion. The average fraction of rays reaching the detector was 80%, which is reasonable taking into account the 5 refractive surfaces of the system with average reflectivity of 4%.

The performance simulations results for the four prismatic designs are summarized in the Fig.5.3. The spherical system A is clearly the worst and it would not be a good choice for the RICH even if its production price would be the best. The chosen comparison method is not the most optimum one, because the angular distribution was too narrow. If a higher σ was used, the designs C and D could have better FOM thanks to the increased f compared to the A and B cases.
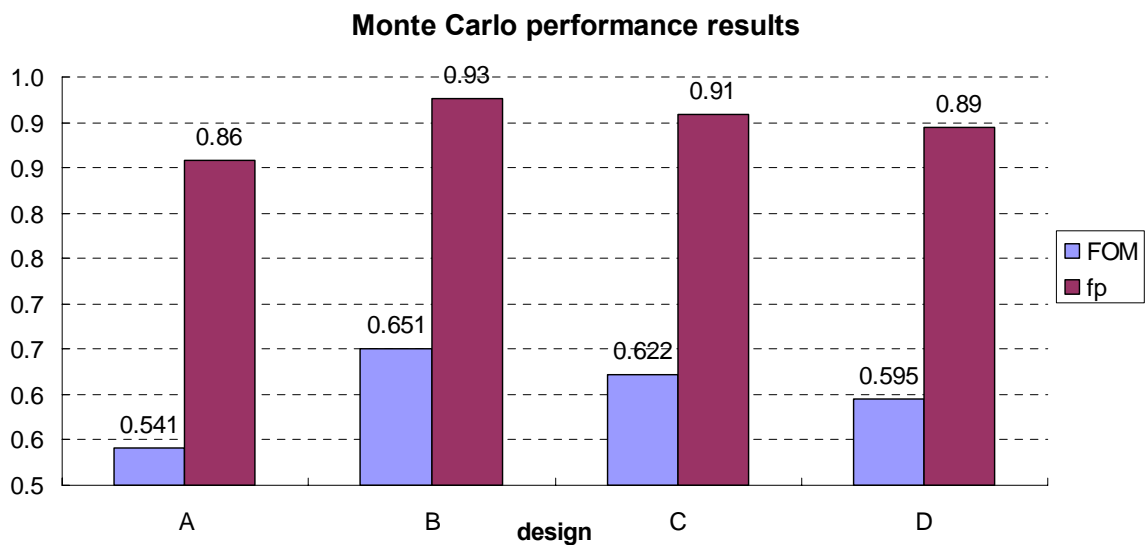
Figure 5.4: *Prismatic designs compared by the figure of merit (FOM) and the fraction of correctly imaged rays (f_p) in relative units.*

The previous figure does not contain any information about the production price, so one could not chose the best system only thanks to it. Considering the very high price of each aspherical surface and the later discovered need for maximum angular acceptance in the horizontal direction, the system D was chosen as the Final Design.

5.3 Final design's acceptance, vignetting and tilt

The chosen angular acceptance defines the apertures for the design and most of the rays within this angular range should strike the correct pixel in the MAPMT. Nevertheless, there was another definition of the acceptance proposed. It should be the angle from the longitudinal axis at which 50% of the rays miss the active area of the photomultiplier.
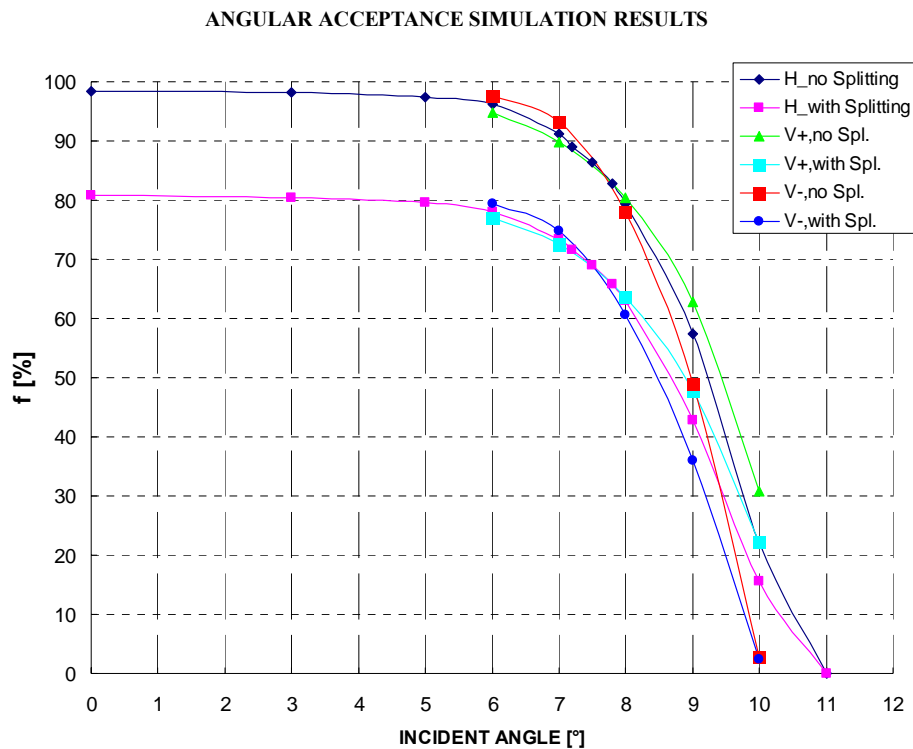
Figure 5.5: *Fraction of rays collected by the photocathode for different incident angles in the horizontal and vertical plane for the final design D.*

The special source files were produced for the acceptance study and the fraction of the rays collected by the MAPMT was recorded with and without using the splitting method. Two signs of the incident angles were investigated for the vertical plane because of the asymmetry caused by the tilt.

The resulting angular acceptance ranges from 9 to 9.5°. This value was used as input parameter for the complex COMPASS detector MC data analysis. The number of lost rings was studied for different locations of the telescopes in the upgraded photon chambers. It was concluded from this study, that the acceptance in the vertical plane should be enough,

but horizontal one could cause problems. The angular distributions are quite narrow, as it was supposed, but their mean value varies considerably throughout the horizontal plane of the RICH1 photon detector surface. The charged particles having higher polar angles while traveling through the RICH1 vessel produce Čerenkov rings with non-zero mean angle. These rings from the low energy particles are imaged mostly in the non-upgraded part of the photon chambers (further from the beam), but still a considerable fraction of them has to be detected by the telescopes.

It was decided thanks to the figure 10.9 in the attachments to tilt the whole telescope by 5 degrees in the horizontal plane. This change shouldn't have a major impact on the imaging properties, because one is only turning the system towards the mean axis of the incident rays, as it was supposed for the field lens to be parallel to it. Due to the mechanical and electronics mounting reasons, 4 telescopes will be tilted together in one horizontal row.
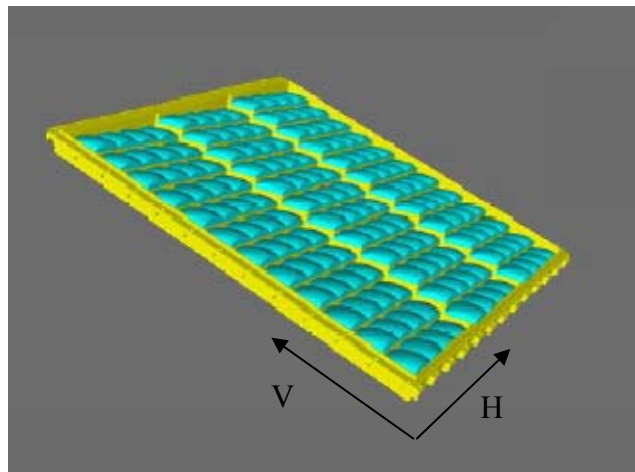
Figure 5.6: *Artistic view of the field lenses in mounted in their frame. Both horizontal (H) and vertical (V) tilts are visible. From [11].*

The final shape of the field lens will not be squared but rectangular of 48x44.8 mm^2. The contraction in the vertical direction is caused by the need to tilt the lenses with relatively thick rectangular edges. The surface covered will remain the same and one gets even slightly better imaging performances, due to the fact that the rays will not travel through the extreme parts of the field lens, but will be concentrated by the neighboring telescope.

The drawback of the rectangular field lens is the unused part of the extreme pixels of the MAPMT, but they should be anyway occupied as the remaining ones because of the imaging aberrations.

The rays aiming the field lens will by partly vignetted by the lens in the subsequent vertical row, see Fig.5.6. Moreover, the lens will have to contain a 2 mm wide step to allow the gas-tight gluing to the mechanical frame. This step will also shield some rays and the combined vignetting effect was simulated thanks to another model using rectangular field lens with an absorbing surface inside as seen on Fig.5.7.
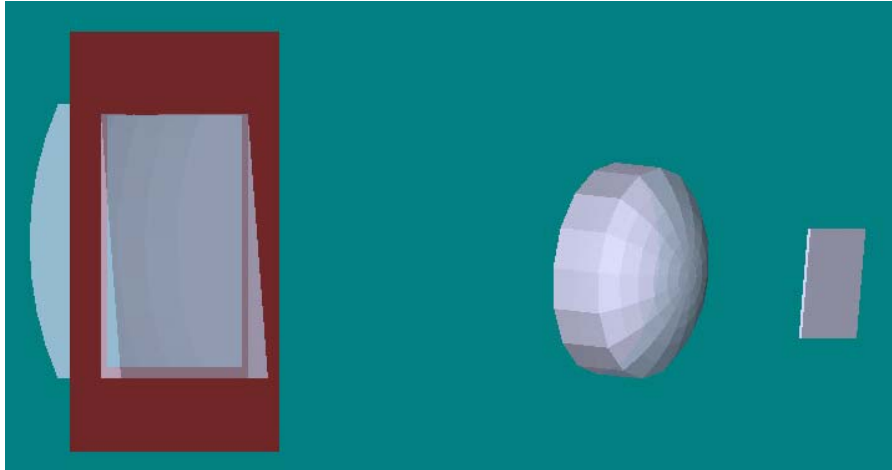
Figure 5.7: *NSC model of the default design with absorbing surface (red) simulating the 2mm gluing step.*

The telescope was then placed in the array with other lenses to simulate the vignetting and a source file with 10^4 rays covering uniformly the field lens area with the standard deviation of 3.3° was used. The neighboring lenses were shifted longitudinally by only 8mm, because the final mounting have not been known yet.
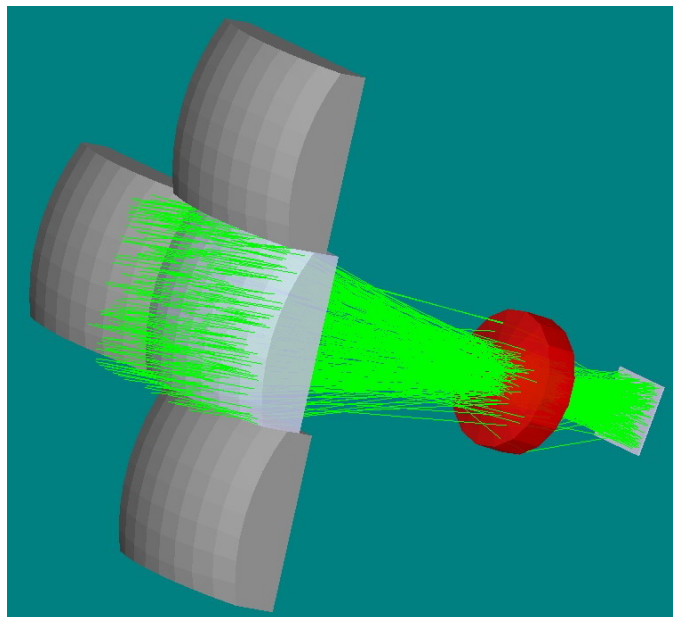
Figure 5.7: *NSC model of the default design with absorbing surface (red) simulating the 2mm gluing step.*

The resulting combined (optimistic) vignetting effect was 3.7%.

6 Sensitivity analysis

It is very important for the functioning of such a large optical array to investigate its imaging performance's sensitivity to different errors. The safe tolerances for the lenses and mechanics production and for the mounting can be chosen accordingly. The overall budget for the effect of the tolerances on the spot size and displacement should be 10% at most.

6.1 "Tolerancing" analysis in ZEMAX

The tolerance analysis in Zemax is accessible only in the SC mode, therefore only the change of the optical parameters available in this mode can be investigated. The "tolerancing" method uses a set of parameters of the design with a tolerance interval defined for each of them.

The simulation varies the given parameters to their limits and saves the corresponding change of the observed imaging quality parameter. Additionally, several (usually 20) Monte Carlo simulations are performed using the Normal distribution of errors for all the defined parameters. The combined effect of the tolerances on the imaging quality can be observed in this way.

The main performance parameter, whose variation can be investigated, is the RMS spot radius averaged for the defined field positions and wavelengths. The image centering in the vertical and horizontal plane was investigated as well. It was necessary to define a special merit function containing just the studied imaging parameter. The CENX and CENY for the central field position were used for the image movement sensitivity.

It wasn't possible to calculate the spot radius in case of larger changes in the design's parameters (too loose tolerances). The design was probably close to total internal reflection for some extreme rays. The RSCE operand calculating the spot radius in the defined field position (usually the image center) had to be used in that case.

6.2 Lenses production and mounting tolerances

Two lists of tolerances that were supposed to be reasonable for this type of design were built first. The lists contained tolerances for the production precision of the lenses and the tolerances for the mechanical housing. Another list combining all the tolerances together was built later.

It was very problematic to make the tolerances analysis with the distant light source definition as it was used in the designing phase. The calculations were very unstable, but it could have been caused by a wrong setting of some parameters. Nevertheless, the light source was placed directly in the mirrors' focal plane and the system's aperture was defined as floating by stop size, which was placed in the last surface of the condensor lens. This approach would not give correct results for optimization, but should be sufficient and stable for the sensitivity analysis.

SURFACE 1	Nominal	Tolerance ±	ΔRMS[µm]	ΔCENY[µm]	ΔCENX[µm]
Radius	54.94 mm	0.5mm	3.3	0	0
Surface irreg.		10fr	0.08	0	0
Thickness	20.813 mm	0.1mm	0.3	1	0
Tilt		0.02°	0.6	2.1	2.1
Decenter		0.1mm	3.1	11	11
Index		0.001	0.5	1.4	0
SURFACE 2					
Radius	infinity	50fr	0.2	0	0
Surface irreg.		10fr	0.08	0	0
Tilt	5°	0.1°	2	13.3	13.3
SURFACE 3					
Radius	20.696 mm	0.06mm	13	2.8	0
Asph. coeff.	-6.13885E-05	5e-7m^{-3}	15	2.3	0
Thickness	19.420 mm	0.1mm	14	0.3	0
Tilt		0.02°	0.04	6	6
Decenter		0.05mm	4	29	29
Index		0.001	14	2.7	0
SURFACE 4					
Radius	-24.964 mm	0.06mm	11	2.4	0
Surface irreg.		10fr	0.4	0.2	0
Tilt		0.02°	0.5	5.7	5.6
Decenter		0.05mm	2.7	32	32
RSS			**31**	**48**	**47**

Table 6.1: *Lenses production tolerances and their maximum effect on the imaging parameters. The maximum numbers are highlighted in red. Reference wavelength 300 nm.*

The square root of the sum of squares (**RSS**) of the individual effects of the errors was made and can be found in the last lines of the summarizing tables Tab.6.1 and Tab.6.2. In fact, some of the tolerances in the previous table are redundant. It is the case of the tilt and decenter of the surfaces. If one tilts a spherical surface, the vertex of the surface (on the axis of the circular aperture) must move too. As there was no practical experience with such tolerances, both of them were put in the list. It was later told to the producers to consider only the tolerances with the worst impact (the surface decenters).

FIELD lens	Nominal	Tolerance ±	ΔRMS[μm]	ΔCENY[μm]	ΔCENX[μm]
Tilt	0	0.05°	0	1.4	1.4
Decenter	0	100μm	0	11	11
Spacing	75.81mm	500μm	3.3	5.4	0
CONDENSOR lens					
Tilt	0	0.05°	0	12	12
Decenter	0	50μm	1	61	61
Spacing (to PMT)	26.84mm	100μm	14	1.2	0
RSS			**14.4**	**63**	**63**

Table 6.2: *Mounting tolerances and their maximum effect on the imaging parameters.*

The basic target of the tolerances analysis was to balance the imaging performance deterioration with the production cost, which decreases with looser limits. The given tolerances must be also achievable by the production method of the aluminum frame. The field lenses will be mounted in a frame separated from the frame housing the MAPMTs. The distance between them will be maintained only by the spacers on the edges of the frames. Thus for example the spacing of the two lenses was set ± 0.5 mm.

As one can see, the main concern for the image displacement is the centering of the condensor lens or respectively of its surfaces. The focusing of the system (distance condensor - PMT) has an important impact on the spot size increase.
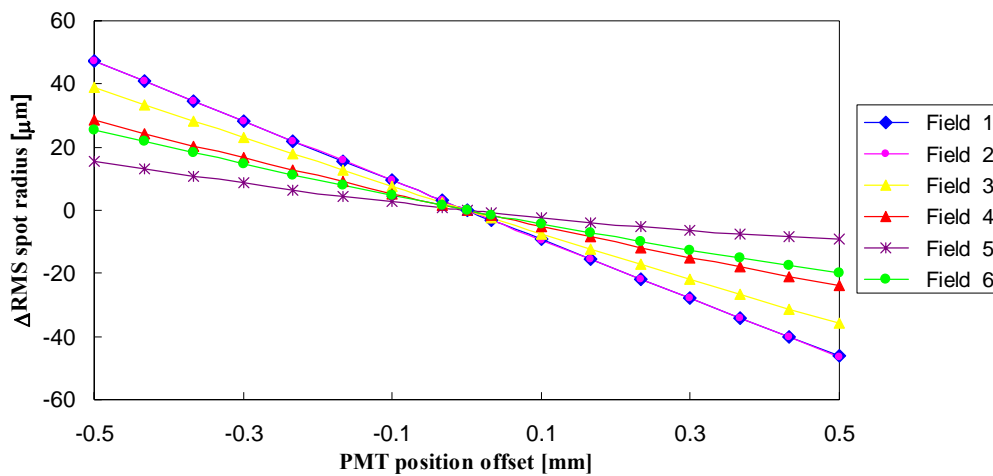
Figure 6.1: *Spot radius change vs. MAPMT entrance window position for different field positions. (Field 1 is in the center of the photocathode).*

It is evident from the Fig.6.1 that the RMS spot radius could even improve for positive offset, but as one expects the worst case, the tolerance of ± 0.1 mm was chosen.

The overall RSS expected change was 35 μm for the spot radius and 80 μm for the displacement in both directions. The resulting standard deviation from the MC simulations was 17 μm for the spot radius and 28 μm for the displacement with respective mean values of 0 and 12 μm.

7 Conclusion

Several possible concentrator system concepts were investigated and the two lens aspherical telescope design with a field and condenser lens was chosen for its proven functionality (in the HERA-B experiment) and thus a shorter development time. A merit function including mechanical constraints and imaging performance targets was composed in the optical design code Zemax.

The design was first optimized for the best performance and then its imaging quality was decreased in steps to match the given mechanical and production cost restraints. It was decided to produce the lenses by grinding and polishing procedure, which is relatively cheep for spherical but expensive for aspherical surfaces. The effort resulted in a non-axial system with a vertical tilt, where the field lens is prismatic on its flat side and the biconvex lens with one aspherical surface.

Performance of different designs was tested by the Monte Carlo Method in the Zemax code using a set of rays simulating an average photon distribution inside the RICH detector. Results were used as a feedback to the optical design. The FOM (Figure Of Merit) specific to the experiment was used to compare the different designs by using collecting and focusing efficiency of the system.

A sensitivity study was performed resulting in production tolerances for the lenses and their mounting system.

The designed system will be produced later in 2005 in 600 pieces and the total cost of the telescope lenses should not optimistically exceed 120 000 euro.

8 References

[1]   E. Nappi, RICH detectors, CERN-EP/99-149

[2]   J. Pretz, COMPASS – status and perspectives, 2003

[3]   M. Laub, Development of opto-mechanical tools and procedures for the new generation of RICH-detectors at CERN, Disertační práce, Praha září 2001

[4]   P. Fauland, The COMPASS Experiment and the RICH-1 Detector, Ph.D Thesis, Mannheim, March 2004

[5]   Novara technology, www.Ntech.it

[6]   D.R. Broemmelsiek, HERA-B RICH light collection system, *Nucl. Instrum. Methods Phys. Res., A* 433 (1999) 136-142

[7]   M. Alekseev et al., Studies for Fast RICH, accepted for Nuclear Inst. and Methods A, January 2005

[8]   M. Bass, Handbook of Optics, McGraw-Hill Inc., New York, 1995

[9]   Zemax User's Guide, www.zemax.com, February 2005

[10]   Artistic View of RICH1, http://pccosrv1.cern.ch/compass/detector/rich/

[11]   S. D. Torre, News from the RICH-upgrade project, CERN March 2005

[12]   E. Albrecht et al., Performance of a cluster of Multi-anode Photomultipliers equipped with lenses for use in a prototype RICH detector, *Nucl. Instrum. Methods Phys. Res., A* 488 (2002) 110-130
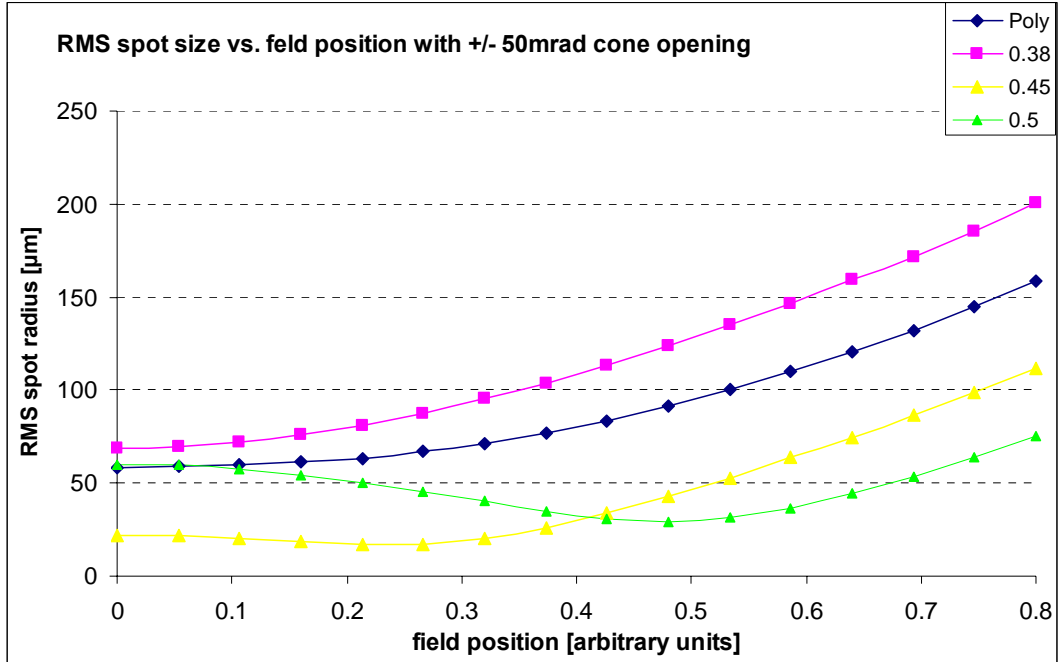
9 Acknowledgements

10   Attachments

Figure 10.1: *HERA B reproduced design's RMS spot size for different wavelengths (in μm) and the weighted average (Poly).*
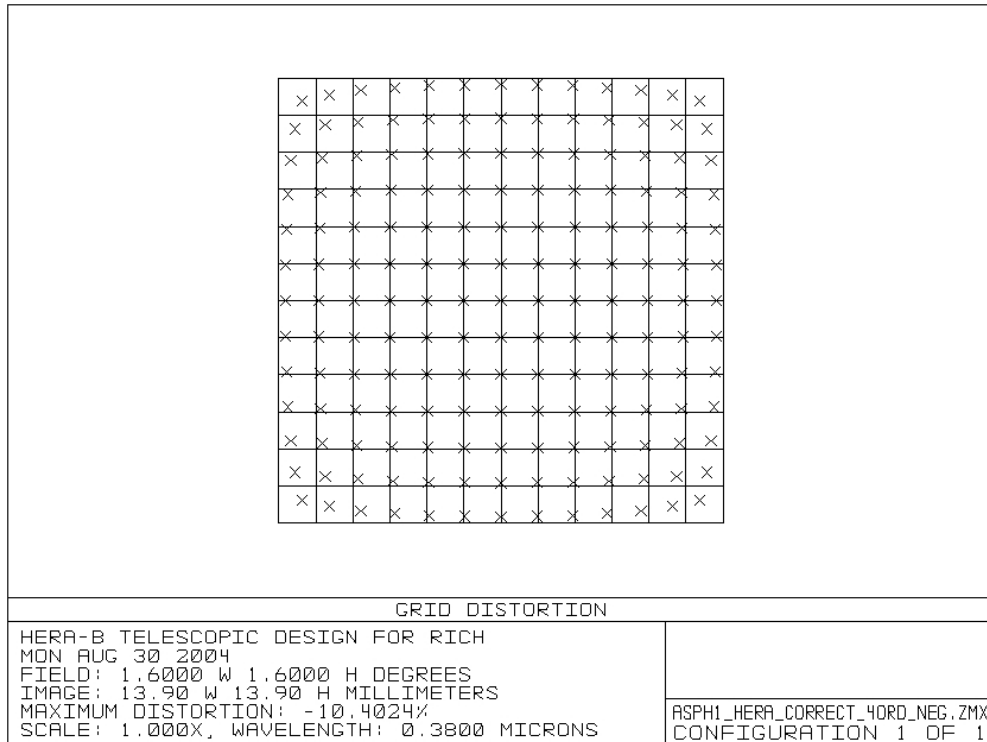
Figure 10.2: *Geometrical grid distortion of the HERA B design.*
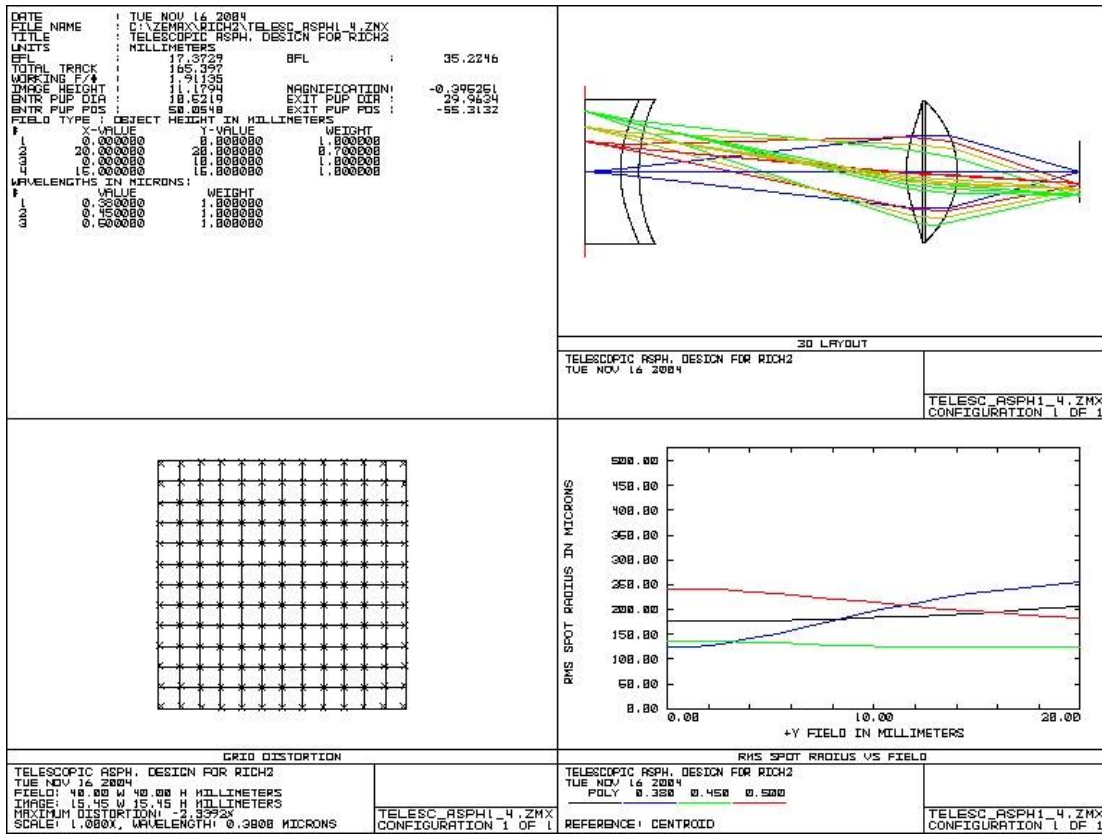
Figure 10.3: *Design report of the first wrong optimization. The wavelength range was not correct too.*
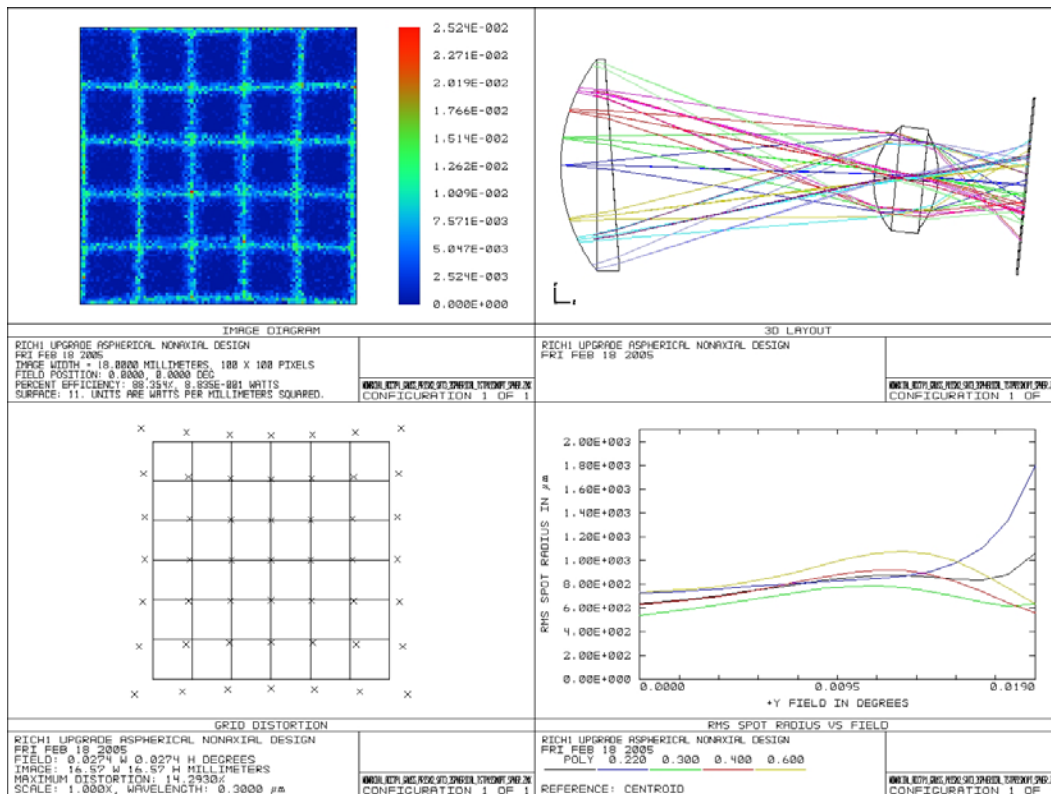
Figure 10.4: *Non-axial prismatic design with ±7.1° acceptance and 0 aspherical surfaces.*
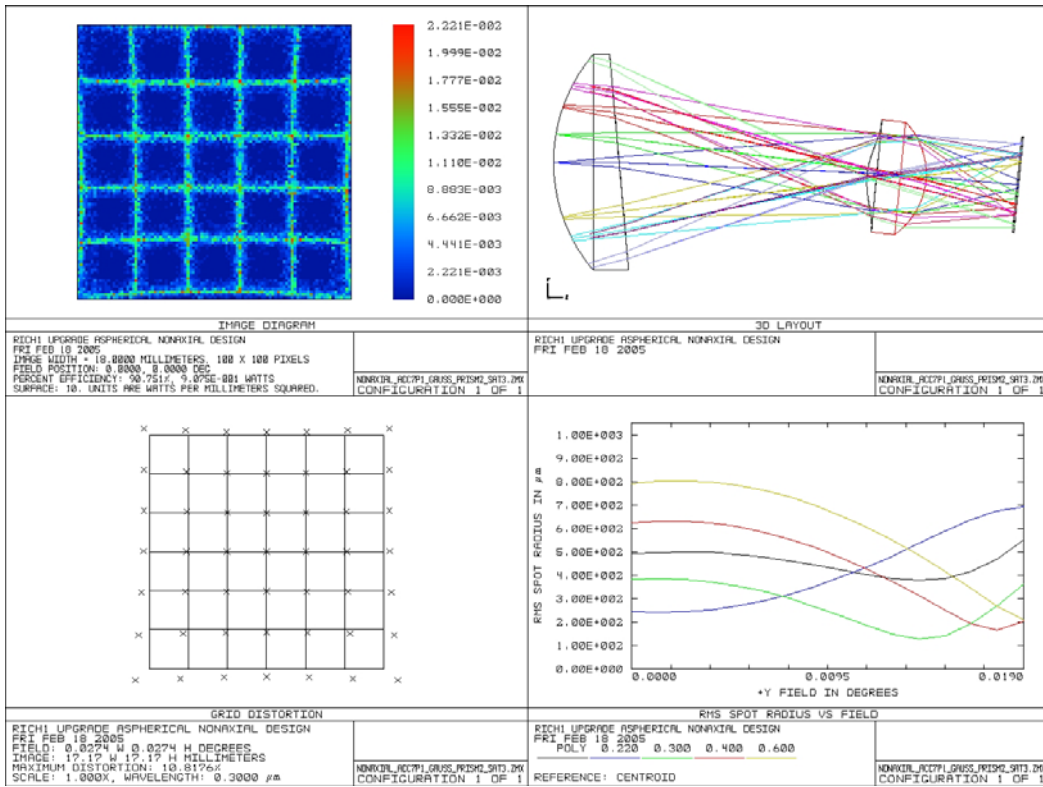
Figure 10.5: *Non-axial prismatic design with ±7.1° acceptance and 1 aspherical surface.*
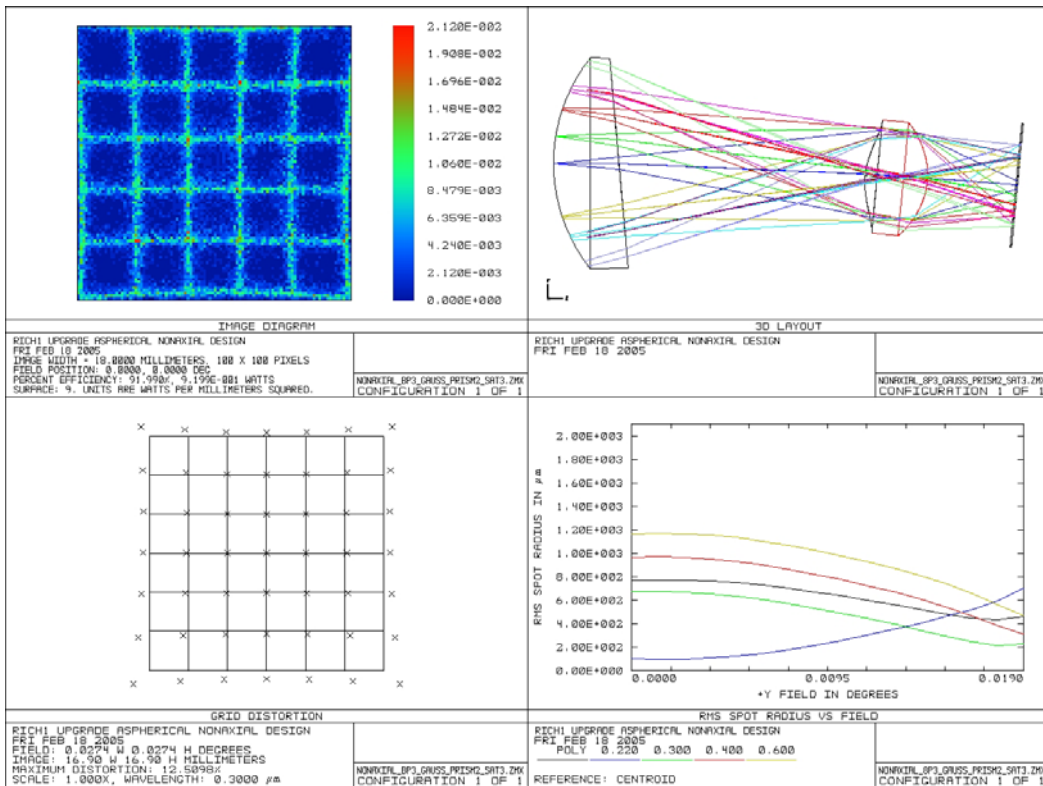
Figure 10.6: *Non-axial prismatic design with ±8.3° acceptance and 2 aspherical surfaces.*
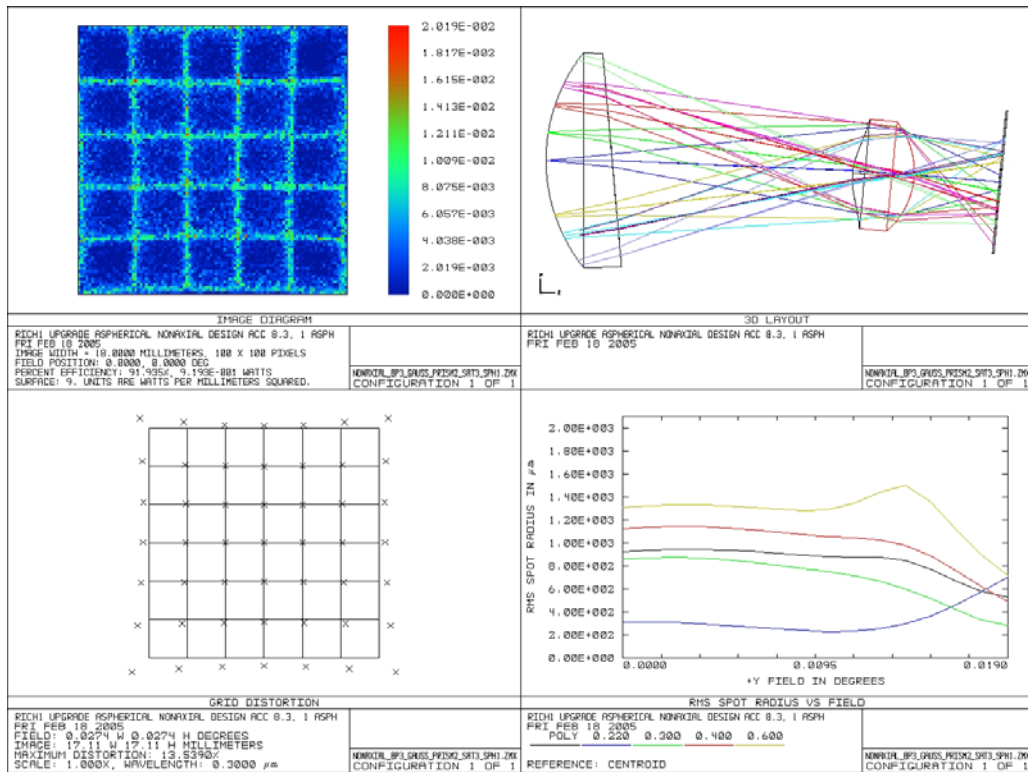
Figure 10.7: *Non-axial prismatic design with ±8.3° acceptance and 1 aspherical surface.*

```
%RAYS GENERATOR FOR ZEMAX MONTE CARLO SIMULATION
namew = 'rays_zemax_rndSGN_';
rows = 10000; % number of rays
sigma_th = 3.3; % degrees
edgex = 0;% rectangle's x edge
edgey = 0;
lenx = 6; % rectangle's x half length
leny = 6;
%---------------------------

y = edgey + 2*leny*rand(rows,1); %uniform distrib.
x = edgex + 2*lenx*rand(rows,1);
z = zeros(rows,1);
n = abs(cos(random('Normal',0,sigma_th,rows,1)*pi/180)); % Gaussian distrib.
m = cos((pi/2 - acos(n)) + rand(rows,1).*acos(n));
m = m.*sign(0.5 - rand(rows,1));
l = sqrt(ones(rows,1)- m.*m - n.*n);
l = l.*sign(0.5 - rand(rows,1));

intensity = ones(rows,1)/rows;
outp = [x,y,z,l,m,n,intensity]; % 3 positions 3 cosines & 1 relative intensity
ros = int2str(rows);
filew = fopen(['C:\MATLAB6p5\work\A_MonteCarlo\',namew,ros,'.dat'],'w');
fprintf(filew ,'%10d    4\n',rows); % 4 for millimeters and lines count
fprintf(filew ,'%10.5f %10.5f %10.5f %10.5f %10.5f %10.5f %10.5f\n',outp');
fclose(filew);
'done'
```

Figure 10.8: *Script for generating source file for Monte Carlo simulations.*
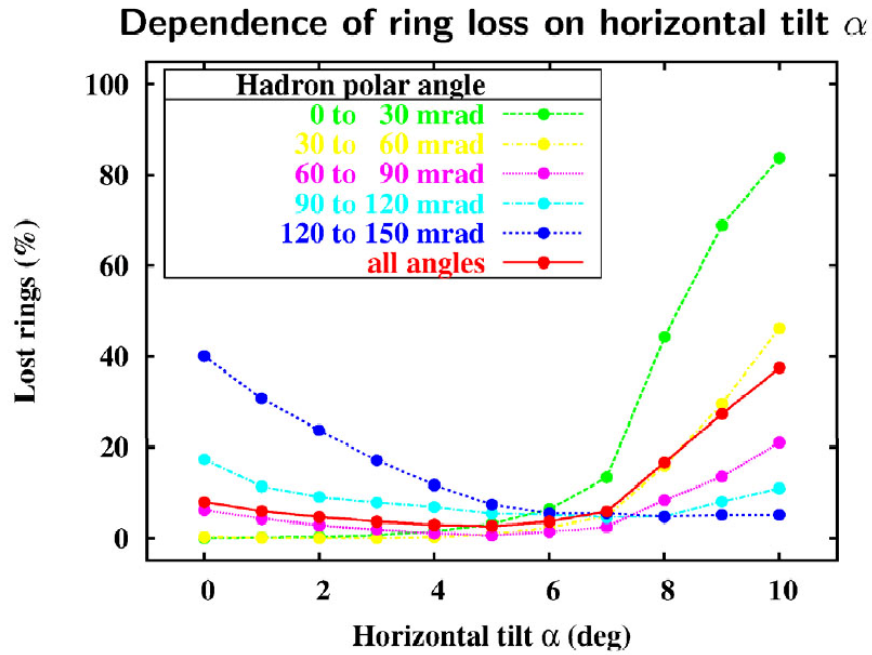
Figure 10.9: *Number of lost Čerenkov rings depending on the telescope's horizontal tilt for different particle track polar angles. [by Andreas Mutter]*
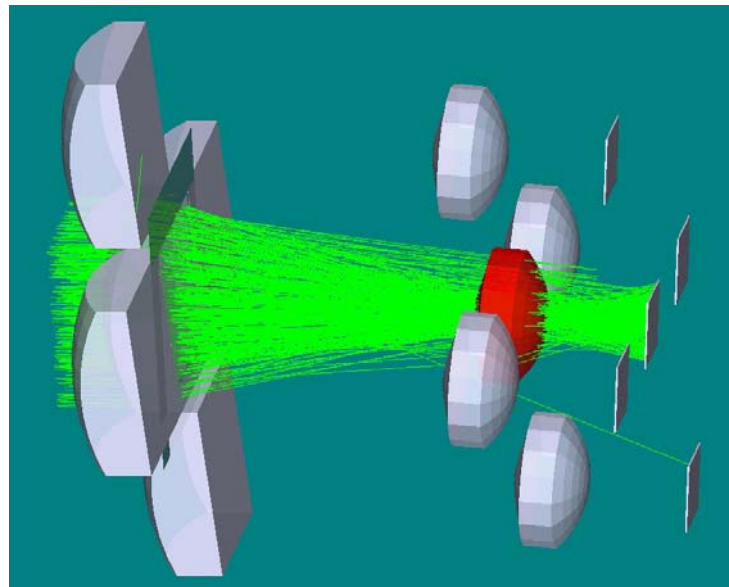
Figure 10.11: *Zemax NSC model of 5 telescopes in the array.*

Parameter	Commercial	Precision	High precision
Wavefront residual	0.25 wave rms	0.1 wave rms	<0.07 wave rms
	2-wave peak	0.5 wave peak	<0.25 wave peak
Thickness	0.1 mm	0.01 mm	0.001 mm
Radius	1.0%	0.1%	0.01%
Index	0.001	0.0001	0.00001
V-number	1.0%	0.1%	0.01%
Homogeneity	0.0001	0.00001	0.000002
Decenter	0.1 mm	0.01 mm	0.001 mm
Tilt	1 arc min	10 arc sec	1 arc sec
Sphericity	2 rings	1 ring	0.25 ring
Irregularity	1 ring	0.25 ring	<0.1 ring

Figure 10.12: *Reasonable Starting Points for Tolerancing a Lens System. From [8].*

Attachment 13: Final design's System / Prescription Data

Title: RICH1 upgrade Aspherical nonaxial design
Date : FRI FEB 18 2005

LENS NOTES: acceptance +/- 8.3
GENERAL LENS DATA:
Surfaces   :   9
Stop   :   1
System Aperture   : Entrance Pupil Diameter = 29000
Glass Catalogs   : SCHOTT MISC CORNING INFRARED HERAEUS
Ray Aiming   : Off
Apodization   : Gaussian, factor = 2.34000E+000
Effective Focal Length :   -38666 (in air at system temperature and pressure)
Effective Focal Length :   -57527.01 (in image space)
Back Focal Length   :   2.847721
Total Track   :   100143.4
Image Space F/#   :   1.33331
Paraxial Working F/#   :   1.33331
Working F/#   :   1.464427
Image Space NA   :   0.3636331
Object Space NA   :   1.45e-006
Stop Radius   :   14500
Paraxial Image Height :   12.97958
Paraxial Magnification :   0
Entrance Pupil Diameter :   29000
Entrance Pupil Position :   0
Exit Pupil Diameter   :   20.47944
Exit Pupil Position   :   -37.77714
Field Type   : Angle in degrees
Maximum Field   :   0.0192333
Primary Wave   :   0.3
Lens Units   : Millimeters
Angular Magnification :   -951.7818

Field Type: Angle in degrees

#	X-Value	Y-Value	Weight
1	0.000000	0.000000	1.000000
2	0.000000	0.005000	1.000000
3	0.000000	0.010000	1.000000
4	0.000000	-0.010000	1.000000
5	0.000000	0.013730	1.000000
6	0.000000	-0.013730	1.000000
7	0.000000	-0.019000	1.000000
8	0.000000	0.019000	1.000000
9	-0.013600	-0.013600	1.000000
10	0.013600	0.013600	1.000000

Wavelengths   : 4
Units: µm

#	Value	Weight
1	0.220000	0.600000
2	0.300000	1.000000
3	0.400000	0.700000
4	0.600000	0.300000

SURFACE DATA SUMMARY:

Surf	Type	Comment	Radius	Thickness	Glass	Diameter	Conic
OBJ	STANDARD		Infinity	Infinity		0	0
STO	PARAXIAL		-	100000		29000	-
2	STANDARD		54.93746	20.81269	F_SILICA	67.88	0
3	STANDARD		Infinity	75.80508		67.88	0
4	COORDBRK		-	0		-	
5	EVENASPH		20.69576	19.42022	F_SILICA	34.67896	0
6	EVENASPH		-24.96372	26.83498		34.67896	0
7	COORDBRK		-	0		-	-
8	STANDARD		Infinity	0.5	F_SILICA	44.8888	0
IMA	STANDARD		Infinity		F_SILICA	45.48032	0

SURFACE DATA DETAIL:

Surface OBJ   : STANDARD
Surface STO   : PARAXIAL
 Focal length :   100000

OPD Mode   :   0
Surface 2 : STANDARD
 Aperture   : Floating Aperture
 Maximum Radius :   33.94
Surface 3 : STANDARD
 Tilt/Decenter :   Decenter X   Decenter Y   Tilt X   Tilt Y   Tilt Z   Order
  Before surface :   0   0   -5   0   0 Decenter, Tilt
  After surface :   0   0   5   0   0 Decenter, Tilt
 Aperture   : Floating Aperture
 Maximum Radius :   33.94
Surface 4 : COORDBRK
 Decenter X   :   0
 Decenter Y   :   -4
 Tilt About X :   5.4604757
 Tilt About Y :   0
 Tilt About Z :   0
 Order   : Decenter then tilt
Surface 5 : EVENASPH
 Coeff on r 2 :   0
 Coeff on r 4 : -6.1388451e-005
 Coeff on r 6 :   0
 Coeff on r 8 :   0
 Coeff on r 10 :   0
 Coeff on r 12 :   0
 Coeff on r 14 :   0
 Coeff on r 16 :   0
Surface 6 : EVENASPH 43.125
 Coeff on r 2 :   0
 Coeff on r 4 :   0
 Coeff on r 6 :   0
 Coeff on r 8 :   0
 Coeff on r 10 :   0
 Coeff on r 12 :   0
 Coeff on r 14 :   0
 Coeff on r 16 :   0
Surface 7 : COORDBRK
 Decenter X   :   0
 Decenter Y   :   1.5
 Tilt About X :   0
 Tilt About Y :   0
 Tilt About Z :   0
 Order   : Decenter then tilt
Surface 8 : STANDARD
Surface IMA   : STANDARD

EDGE THICKNESS DATA:

Surf   X-Edge   Y-Edge
 STO 100011.737911 100011.737911
  2   9.074783   9.074783
  3   75.805082   75.805082
  4   3.848020   3.848020
  5   8.567590   8.567590
  6   33.839583   33.839583
  7   0.000000   0.000000
  8   0.500000   0.500000
 IMA   0.000000   0.000000

SOLVE AND VARIABLE DATA:
 Curvature of 2   : Variable
 Thickness of 2   : Variable
 Semi Diameter 2   : Fixed
 Thickness of 3   : Variable
 Semi Diameter 3   : Pickup from 2
 Parameter 3 Surf 4 : Variable
 Curvature of 5   : Variable
 Thickness of 5   : Variable
 Parameter 2 Surf 5 : Variable
 Curvature of 6   : Variable
 Thickness of 6   : Variable
 Semi Diameter 6   : Pickup from 5

ELEMENT VOLUME DATA:
              Volume cc Density g/cc   Mass g
Element surf 2 to 3   54.922002   2.200000   120.828404
Element surf 5 to 6   12.958730   2.200000   28.509206